Advancing Atom Interferometry with a Bloch-bands Approach

Katherine E. McAlpine

A dissertation
submitted in partial fulfillment of the
requirements for the degree of

Doctor of Philosophy

University of Washington

2019

Reading Committee:

Subhadeep Gupta, Chair

Boris Blinov

Sanjay Reddy

Miguel Morales

Program Authorized to Offer Degree:
Physics

University of Washington

Abstract

Advancing Atom Interferometry with a Bloch-bands Approach

Katherine E. McAlpine

Chair of the Supervisory Committee:
Subhadeep Gupta
Department of Physics

This work presents experiments and theory on "magic depths" in Bloch oscillation acceleration pulses and the implications for advancing atom interferometry. For a particle in a sinusoidal potential, we define the magic depth as the depth where there is a vanishing first derivative of its average energy[1], occurring only for excited bands. A Bloch-bands picture demonstrates that this average area is proportional to the diffraction phase shift experienced by a particle undergoing Bloch oscillations. A vanishing first derivative permits the phase to be significantly more stable against unavoidable light intensity fluctuations, creating new opportunities for the use of Bloch oscillations within atom interferometers.

[1] Averaged over the first Brillouin zone.

TABLE OF CONTENTS

LIST OF FIGURES

5.3 (a) Space-time diagram for a Mach-Zehnder interferometer with 1 BO applied to the upper path. The blue arm is the one which has been accelerated by Bloch oscillations of varying depths. Pulses affecting the upper (lower) arm only are highlighted in purple (pink). Pulse affecting both arms are highlighted in gray. Intensity profiles of the pulses are shown below in green. The representative interferometer shown has free evolution times of $10\,\mu$s and $630\,\mu$s for the first and second halves of the interferometer, respectively. The fractional population in the $|6\hbar k\rangle$ path as a function of the phase of the final recombination pulse with each point being the average of three measurements is shown in (b) and (c). For (b), one BO is performed in the first excited band ($b = 1$) near the magic depth at $U_0 = 11.2E_r$. For (c) the BO is instead performed in the ground band ($b = 0$) at a depth near the first excited band's magic depth ($9.7E_r$). The best fit sinusoids are shown. The phase of the fringe as extracted from a sinusoidal fit is plotted as a function of the depth of the BO in (d). The phase measurements are in good agreement with the phase calculated by our Bloch-bands model. The ground band is shown in red and the first excited band shown in blue. The first excited band exhibits a local maximum and thus the magic depth feature whereas the ground band does not exhibit any local extrema. In (e) the visibility of the fringe fits as a function of depth for the data collected in (c). For the first excited band, $\Delta/\Gamma = +3500$ and for the ground band $\Delta/\Gamma = +1300$. For both bands, $\dot{\delta} = 2\pi \times 83\,\text{kHz/msec}$ 65

5.4 Diffraction phase versus lattice depth U_0 for various band numbers and number of Bloch oscillations with a theory curve from a Bloch-bands calculation. (a) shows b=1 with 0, 1, 2, 3 Bloch oscillations shown in purple (triangles), blue (circles), and green (squares), respectively. The location of the magic depth as defined as $\frac{\partial\langle E\rangle}{\partial U_0} = 0$. In (b), BO with $b = 2$ (orange, circle) and $b = 3$ (black, triangles) are shown. Note that in (a) the "1 BO" data is also shown in Figure5.3(d). For all data shown $\Delta/\Gamma = +1300$, $\dot{\delta} = 2\pi \times 83\,\text{kHz/msec}$, and intensity ramp times are $300\,\mu$s. 67

GLOSSARY

BEC: Bose-Einstein condensate

BO: Bloch oscillation

CI: Contrast interferometer

IFM: Interferometer

MOT: Magneto-optical trap

MZ: Mach-Zehnder

LZ: Landau-Zener

ODT: Optical dipole trap

ACKNOWLEDGMENTS

It takes a village to raise a child so with that I would like to thank my village. I am currently in extreme karma debt to my friends and family for their support, especially recently.

I would like to acknowledge the path that brought me to this point. I grew up in a weird area in Florida filled with retirees, mermaids, and adventure. There wasn't much to do and so I got used to finding novelty in repetition, which I think helped me in my physics work. I was fortunate enough that my mom helped to get me into the "Gifted Program." This meant that many of my classes were extremely small.

I chose to take physics because I liked math. However, I wasn't getting what I wanted out of the class and had planned to drop it. My physics class wasn't the friendliest environment. My teacher claimed to not hear the frequency of women's voices due to shell shock from the Vietnam war and would often unapologetically ignore women who asked questions.

One day in class we were doing a physics problem which attempted to model the depth a diver would reach after jumping into water from a diving board. A Newtonian or energy conservation model can be used, and I was asking if that was always the case for any physics problem. As I put together my question, a male student hurled insults at me. I tried to ignore him, but I ended up crying. How embarrassing! I'll give my teacher the benefit of the doubt and say perhaps he didn't know what to do, which as nothing. I ended up sticking with physics ostensibly because I wanted to

outdo him on the advanced placement (AP) exam. He ended up dropping the class the next semester because he did not like electricity and magnetism and I finished the course and passed the AP exam.

I can't say I would want to stick with something to outdo someone again, but I am glad I did. Despite ostensibly only staying in physics to outdo him, there were probably other reasons. Physics has been appealing to me because it involves two interests of mine: understanding the universe and organization. It pleases me to be able to approach both profound and simple questions in an organized manner.

I went to New College of Florida after graduating from high school. If you haven't heard of it, it is a small liberal arts college in Sarasota, Florida, which is famous for not assigning grades and barefoot students. The lack of grades allowed me to do more project-based work, which was a great learning experience. I appreciated the three physics professors there. Don Colladay taught many of my classes and was always willing to help me with physics questions. I also benefited from his clear handwriting. I enjoyed the patient and caring way George Ruppeiner would explain physics. I appreciated the efforts he made to drive me and a dear friend and fellow physics student Yanet Estrella to the University of South Florida's physics colloquia. Finally, I would like to thank my thesis advisor Mariana Sendova for her work in teaching me about optics and spectrscopy and guiding me through my first thesis process. I could feel her faith in my work, and it was motivating.

One unique aspect of my experience at New College was that most of the people graduating with a physics degree with me were women. To Kat Kiker, Emily Myers, and Sonali Gupta, I thoroughly enjoyed working on physics with you.

During my time at New College, I worked at JILA at CU Boulder as a part of the

REU program with James Thompson. There, I was more exposed to the beautiful world of atomic physics. I learned what atomic physics lab life was like, and it seeded a goal in me to be able to design and run complicated experiments to explore quantum behavior.

I came to the University of Washington (UW) in the summer of 2013. I am lucky that I genuinely liked and connected with many people in my cohort and felt a real sense of community with them. My office-mate, Rachel Osofsky was a source of inspiration. She is both calm and productive, two qualities which are no small feat to balance. It made working on physics with her incredibly fun, and I often felt I was in a state of "flow" with her. I also grew close to Tyson Price, someone with a fantastically energetic approach to physics. Fantastical energy is easy for me to relate to. I appreciated the way Chris Baldwin with both incredibly skilled as a physicist but equally kind.

Finally, last but not least, Alaina Green. Alaina also joined the Gupta lab and has been a bountiful source of intelligence, love, openness, and support. We had thrice-weekly morning gym appointments where we would share all- physics, relationships, and life. I am lucky to know her and having her support through the thesis-writing process has been invaluable. While at UW I co-founded a group called Physics for Inclusion and Equity (PIE). I am grateful for the experiences there, especially the book club meetings and happy hours. My work in PIE helped me stay connected to my social and moral values, which was an energizing experience. I hope the topics of inclusion and equity stays on the table in the department after I leave (at least do a book club, y'all!).

I am grateful for the work of the grad student union, UAW 4121 to reduce fees,

improve healthcare, and increase our pay. I am thankful that I was generally able to see a doctor for free, allowing health issues to not balloon and get in the way of my goals. Living in Seattle is incredibly expensive and finding housing can be challenging- we make about $2,400/month and the studio price for grad student on-campus housing is about $1,400/month, to put it in perspective. I hope the essential work performed by grad students will one day be appropriately valued.

I acknowledge the help of my tireless advisor Subhadeep Gupta. I am inspired by the care he uses in his work and the skills he has built over the years of doing physics, leading to impressive intuition. I appreciate the time he has taken to edit my work and give guidance and feedback on experiments.

In the experiments in this thesis, I primarily worked with Daniel Gochnauer. I appreciate the contributions from his meticulous work. I am grateful to the work of my former labmates, including Ben Plotkin-Swing and Alan Jamison. A few older department members were wonderful mentors to me, including Ryan Bowler, Spencer Williams, and Carolyn Auchter. Thank you for the "netwerking" skills, skateboarding sessions, and pies, respectively.

Recently, the grad students Tahiyat Rahman and Anna Wirth joined the Gupta lab and their presence definitely brightened the lab atmosphere. I have enjoyed getting to know y'all and I'm excited to see where you take the project.

I thank my committee for taking the time to support my work.

I met a wonderful group of people outside of grad school, including (in alphabetical order) Yazan Aldehayyat, Eric Champe, Zening Chen, Courtney Cox, Priya Deshpande, Stephanie Giola, Dan Kelly, Jessica Kopp McCorkle, Erin Krengel, Peter Krengel, Jayant Krishnamurthy, H. Chris McCorkle, Emily Newcomer, and Deedee

Sun. I am prone to tunnel vision, so having a little world free of grad school demands was great. My friends have always been incredibly supportive of my work. After my defense, Steph, Courtney, and Deede even put together a surprise party filled with my favorite things including grocery store cake, negronis, macarons, 2000's rap classics, and pictures of my cats. They also put together the sweetest slide deck ("Bloch bands may oscillate, but your friends will never waiver."). Also, I am deeply indebted to Steph for a variety of reasons, including the fact that she waded through and edited parts of my thesis.

Thank you to my parents and grandma (Mimi) for caring for me and shuttling me around to all my activities throughout my childhood. After they visited for my PhD final, Steph remarked that she was impressed with how proud they were, and mused that it might be a source of my confidence. I'm not sure if that is the case, but either way, "Thank you." While I'm circling back to childhood, thank you to my dear friend and partner and crime Kindo Lee for all the fun in the Confraternity of Christian Doctrine (CCD) classes, brain bowls, and just drifting around town in your Rabbit.

Last but obviously not least, I would like to thank my dear fiancé Kevin Fisher for your marathon-level of support through this process. Thank you for the coffees in bed, the nights you cooked AND cleaned, being available for fleshing out problems, bringing food to my general and final exam, editing my thesis when it was sad garbage, generally taking care of me, and being my partner. I am so excited for our future adventures and I hope I can support you in the way that you've supported me.

DEDICATION

to Marge and Willow

Chapter 1

INTRODUCTION

1.1 Standing Waves and Atom Interferometry

This work begins with discussing an essential piece of physics for atom interferometry: the interaction of standing waves of light with matter. A standing wave of light is composed of two counterpropagating waves. When these waves are added together, there exists nodes which are equally spaced points in space where the wave sum is always zero. The relevant property of standing waves for atom interferometery is that standing waves of light can efficiently reflect atoms. It would be strange if this were ordinary behavior. You might need to avoid putting two lamps too close, otherwise some photons from the lamps could form a standing wave that could give you a jolt when passing between them.

Here lies an important implication of "standing waves of light can reflect atoms." If a standing wave's nodes are moving in your frame and it were reflecting an atom, you would see the atom as accelerating. In such a way, could this utilization of standing waves become a new form of transportation? Rather than boarding a train to move from point a to b, could we merely step between two counterpropagating light sources composed of many laser beams. Of course this would mandate careful tuning of the frequencies and intensities in order to ensure one's entire body is coherently accelerated. Such travel may be dangerous if the "train" conductors do not get the resonance right.

I was quite surprised to hear that standing waves reflect atoms when my advisor

Professor Subhadeep Gupta provided a standard introduction to atom interferometery, something to the effect of:

> A typical light interferometer includes splitting light into multiple paths, reflecting the paths such that they recombine, and observing the interference. In this case, the light is the wave, and the matter plays the role of the momentum manipulator. In an atom interferometer, the roles are reversed. The light pulses split the matterwaves, reflect the atoms such that they recombine, and read out the final interference.

This was likely followed with a discussion on the merits of the particular interferometer used in our group, such as the quadratic scaling with momentum or vibration sensitivity. I, however, was distracted by formulating the many questions I had about this process.

I imagine that I wondered whether or not the fact that standing waves reflect atoms could be predicted classically, i.e. by treating the atoms as particles? Perhaps atoms in a standing wave can be imagined like small spherical beads in an egg carton. Imagine somehow one was able to initialize all beads to be at the same speed. Would they all turn around, and then would that be the way to predict reflection? I can certainly imagine beads sloshing around in an egg carton, reflecting when they've turned their kinetic energy into potential energy.

In fact, this particle model does not predict that atoms can be reflected by standing waves of light. For example, consider the situation where the potential energy created by the standing wave was smaller than the kinetic energy of the atoms. In that case, the atoms would not reflect but rather keep moving in the same direction and hop from site to site in the egg carton. However, it is known that standing waves can reflect atoms whose kinetic energies are larger than the maximum potential

energy.

Another issue with the particle model is that the atom reflection process can be velocity-sensitive in the case of Bragg reflection, as shall be detailed in Section 2.1. One takeaway from that section is that for an atom to reflect from a standing wave, it needs to be at a particular velocity. However, classical particles in a potential well can eventually reflect given any initial velocity, assuming their kinetic energy is less than the potential depth.

The key to understanding that standing waves of light reflect atoms is seeing atoms as waves and thus to even make correct qualitative predictions, a quantum model is absolutely necessary. Once this conceptual leap is made, the reflection can be described using similar formalism to Bragg reflection of light off of crystals. The reflection of atoms from standing wave potentials can be seen as a probabilistic process; as a matterwave moves along a standing wave's longitudinal direction, there is a periodic probability that the wave will reflect. Eventually, the probability of reflection approaches unity. Of course since the reflection of atoms from standing waves is not ordinary behavior, certain conditions must be met. These conditions are detailed in Chapter 2 and 3.

1.2 Thesis Overview

The prior section introduced an essential piece of physics to atom interferometry: the reflection of atoms from standing waves. This section will provide a brief introduction of atom interferometery and use it to explain the context of the bulk of what is presented in the thesis.

In 2018, the Müller group at Berkeley obtained the current most precise measurement of the fine-structure constant (α) through a measurement of the recoil energy of cesium (Cs) in their atom interferometer, obtaining an uncertainty of .2 parts-

per-billion (ppb)[1]. The recoil energy is defined as the energy of a particle after absorbing one photon. The fine-structure constant sets the electromagnetic coupling strength for matter.

Before this 2018 measurement, the most precise measurement of the fine-structure constant came from entirely different measurement. The Gabrielse group at Harvard measured the anomalous part of the g factor of the electron. QED tells us that the g factor is equal to a power series expansion in α. The calculation that connects the g factor and α is complicated, evinced by the fact that the paper reporting the α calculation[2] came two years after the g factor measurement[3]. Through providing a theory-free measurement of the fine-structure constant, atom interferometry is able to test the theory which connects these two quantities, which includes QED and the standard model. More on this in Section 1.3.1.

Indeed atom interferometry is a burgeoning field in quantum metrology. Research groups around the world with various interferometer geometries are developing atom interferometers for purposes including measuring gravity and gravity gradients[4], measuring atomic polarizabilities[5] and performing rotational sensing[6]. Atom interferometry is a sensitive way to measure matter's properties.

A long-term goal in the group is performing a precision measurement of α with our contrast interferometer, described in detail in Section 1.6. In 2014 the first Ytterbium (Yb) atom interferometer was up and running in the UW physics building basement[7]. We continued to develop our contrast interferometer and in 2017 we demonstrated large momentum separation in the arms of our interferometer[8]. Along the way, we needed to develop a better understanding of a systematic effect called diffraction phases.

A diffraction phase is a shift on our signal due to the light pulses used for accelerating the atoms. This systematic affects a variety of interferometers and it is

important to be able to intuit its behavior. Much of my work was related to developing a way to predict diffraction phases from the perspective of band structure. We were able to use those predictions to discover a new way to minimize diffraction phases through operating at so-called "magic depths" which is the topic of Chapter 5. Note that in this thesis, I intend to use the term "diffraction phases" to refer to the phase shift a particle experiences in a diffraction pulse. The term "lattice-induced phase shift" means the same thing but is used when describing the phase shift from Bloch oscillation pulses. The two terms are interchangable.

1.3 Recoil Measurements

The prior section motivated measuring the fine-structure constant through a recoil frequency measurement in order to test QED. This section will provide more details on the fine-structure constant, the g-2 measurement, and recoil measurements.

The fine-structure constant

One way to define the fine-structure constant in SI units is:

$$\alpha = \frac{1}{4\pi\epsilon_0}\frac{e^2}{\hbar c}, \tag{1.1}$$

where ϵ_0 is the permittivity of free space, e is the elementary charge, $\hbar$ is the reduced Planck's constant, and c is the speed of light.

A clear way to see it as the strength of electromagnetic interactions is its definition in natural units, where $\epsilon_0 = c = \hbar = 1$:

$$\alpha = \frac{e^2}{4\pi}. \tag{1.2}$$

In these units, α is related only to e, which quantifies the coupling strength between an electromagnetic field and a charge.

One place of interest that the fine-structure constant appears is in corrections to the Hamiltonian for hydrogen-like atoms. Specifically, the kinematic relativistic correction yields a perturbation proportional to α^2. The spin-orbit coupling energy shift, which comes from the coupling between an electron's spin and orbital momentum, shifts the Hamiltonian by a term proportional to α^4. The Lamb shift, proportional to α^5, comes from the quantization of the electric field.[9] The desire to understand the Lamb shift was an impetus for developing QED and making the associated measurements to support the theory.

1.3.1 g-2 Measurement of the Electron

The most precise measurement of the fine-structure constant comes from the anomalous part of the g factor of the electron. The g factor is a dimensionless quantity which is proportional to the ratio of a particle or system's magnetic moment to its angular momentum. For the electron, it is the coefficient in the equation for the magnetic moment of the electron, $\mu_e = -g\mu_B\vec{S}/\hbar$, where $\vec{S}$ is the electron spin, and $\mu_B = e\hbar/2m_e$ is the Bohr magneton. The Dirac equation predicts that g = 2, but quantum electrodynamic (QED) corrections predict that it deviates from 2 and measurements show that its magnitude is actually 2.00231930436182[2]. The Dirac equation treats the electron quantum mechanically and relativistically. QED corrections come from quantizing the electric field.

Dirac theory also predicts that the change in energy ΔE for a spin flip in a certain magnetic field $\vec{B}$ is equal to the cyclotron frequency $f_c = e|\vec{B}|/(2\pi m_e)$ multiplied by h. The cyclotron frequency is the number of cycles per second that an electron completes as it rotates in response to a magnetic field which is perpendicular to its velocity. This experiment essentially measures the cyclotron frequency and spin

flip energy and compare these two values. The energy difference is due only to the anomalous part of the electron's magnetic moment, and thus a calculation of g can be made[2].

QED tells us that the g factor is equal to an asymptotic expansion of α:

$$\frac{g}{2} = 1 + \sum_{i=1} C_{2i} \left(\frac{\alpha}{\pi}^i\right) + ... + a_{\mu\tau} + a_{hadronic} + a_{weak}, \tag{1.3}$$

where C_i are constants, $a_{\mu\tau}$ come from QED, and $a_{hadronic}$ and a_{weak} are very small hadronic and weak contributions[2]. Calculating α from g involves inverting this relation. The calculation is one of the most complex calculations undertaken in QED, using tenth order perturbation theory. Comparing a more precise measurement of α against that which was calculated from QED will test the theory at an unprecedented level.

Testing whether or not QED holds true in this highly perturbation regime can test other physics models. For example, the calculation of α from g relies on hadronic and muon loops. Unlike lower order terms, their contribution must be inferred from low energy electron to hadron scattering data and quantum field theory rather than being calculated directly. This is because quantum chromodynamics (QCD), unlike QED, is nonperturbative. Thus an independent measurement of α can test these theories.

1.3.2 Interferometry and α

Interferometry is a powerful experimental technique which examines the way that waves interfere as a consequence of the differential phase between the interfering waves. This phase difference can be mapped to a property of the wave trajectory. For a simple example, one could direct laser light onto a strand of hair and look at the spacing of interference fringes. The larger the spacing between the fringes, the smaller

the hair diameter is, which can be shown with Fraunhofer far-field diffraction theory. In a much more complicated experiment, LIGO examined the change in interference of light due to gravitational waves, which is caused by a change in path length on by an impressively small factor of 10^{-21}.[10]

To understand how interferometry can be used to measure the fine-structure constant, consider another way to formulate α:

$$\alpha^2 = \frac{2R_\infty}{c}\frac{h}{m_e} = \frac{2R_\infty}{c}\frac{h}{m_X}\frac{m_X}{m_e}, \tag{1.4}$$

where $R_\infty = \frac{m_e e^4}{8\epsilon_0^2 h^3 c}$ is the Rydberg constant with an infinitely massive nucleus, m_e is the mass of an electron, and m_X is some test mass. Since h/m_X is the quantity which is known least precisely, it is what these recoil measurements seek to measure.

1.4 Atomic/Molecular/Optical and Solid State Physics

Optical lattices can simulate the ionic cores of crystals and thus the models of solid-state physics can be cleanly studied in atomic physics systems. A variety of potential landscapes can be created with light by tuning parameters such as light intensity, frequency, and geometry. The interactions of particles within these optical lattices can often be tuned through magnetic or optical Feshbach resonances.

Of interest is gleaning the band structure associated with a potential (more on band structure in Section 2.2). For example, a Landau-Zener-Stückelberg interferometer[11] can be used to map the band structure of potentials by examining the phase shift of an atom when it completes a Landau-Zener process (more on Landau-Zener processes in Section 2.3). To understand the topology of graphene, an analog system involving graphene-type hexagonal optical lattices is used to make an interferometric measurement of Berry flux in momentum space.[12]

Of particular importance to this work is Bloch oscillations (BO), which describe the motion of particles both in a periodic potential and experiencing a constant force. It was first predicted for electrons in a crystal lattice by Felix Bloch in 1928[13]. However, observing Bloch oscillations proved difficult because the coherence of Bloch states was generally destroyed by scattering. It was not until 1993[14] that Bloch oscillations could be observed in a superlattice, which is a periodic structure of multiple materials. The coherence was increased when a bias field led to enhanced coupling between wells and a delocalization of the electron and hole wavefunctions.

Soon after, Bloch oscillations were observed for ultracold atoms in optical lattices [15, 16, 17] and they are now used for high efficiency momentum transfer in atom interferometery.[18]

1.5 Bose-Einstein Condensates

We use a Bose-Einstein Condensate (BEC) atom source for our experiments so it is worth explaining some of its physical properties. At low phase space density, particles have many states available to occupy. They rarely occupy the same quantum state and thus behave classically. From statistical mechanics, it is known that when a system of bosons reaches a critically high phase space density, a phase transition occurs such that a non-negligible percentage of the atoms occupy the ground state. When atoms are cooled to a high phase space density, quantum statistics are needed to model their behavior. For bosons, this means they avalanche into the ground state, forming a BEC.

Quantum effects arise when the particle density (number per unit volume), n, reaches a value

$$n = \frac{2.6}{\lambda_{dB}^3}, \tag{1.5}$$

where λ_{dB} is the thermal de Broglie wavelength

$$\lambda_{dB} = \frac{h}{\sqrt{2\pi M k_B T}}, \tag{1.6}$$

where h is Planck's constant, M is the mass of an atom in the gas, k_B is Boltzmann's constant, and T is the temperature of the system.

Equation 1.5 shows that quantum effects occur when the inverse density of one particle becomes comparable to the volume associated with its de Broglie wavelength. The de Broglie wavelength gives a length of space over which the particle will be delocalized. When this is on the order of interparticle separation, the particles become less distinguishable.[9]

Forming a BEC was theorized to happen by Albert Einstein and Satyendra Nath Bose in the 1920's. It was experimentally realized in 1995 with ^{87}Rb atoms, for which Eric Cornell, Wolfgang Ketterle and Carl Weiman were awarded the Nobel Prize in 2001.[19] To cool the atoms to sufficiently low temperatures, laser cooling is used. Laser cooling is a technique where an atom is slowed by absorbing photons from a laser beam traveling in the opposite direction of the atom. After being laser cooled, the atoms were loaded into a magneto-optical trap which uses magnets to ensure that atoms preferentially absorb light that sends them back to the center of their trap. Then the atoms were transferred into a magnetic trap[1] where they were evaporatively cooled to quantum degeneracy. More technical details on some of the cooling techniques mentioned can be found in this thesis in Chapter 3.

A BEC is special because it a macroscopic, massive quantum object. Its coherence properties and specifically its narrow momentum distribution, are of particular help to our experiment because of the velocity selectivity of the Bragg process.

---

[1]Magnetic traps are not used in our lab. In our experiments, we instead use optical dipole traps (Section 3.3.3).

1.6 Contrast Interferometry

This section describes the contrast interferometer my group uses to perform a measurement of the fine-structure constant. It is described in great detail in my former lab mate's theses[8],[20], Deep's thesis[21], and in the papers published from my lab[7][8].

We use a ^{174}Yb BEC atom source in our three-arm interferometer, shown in Figure 1.1. A Kapitza-Dirac pulse separates an atom cloud into a superposition of three momentum states, $|\pm 2\hbar k\rangle$ and $|0\rangle$. This standing wave pulse is described with different physics than a Bragg pulse or a Bloch oscillation pulse, as described in Chapter 2. This much shorter pulse spatially modulates the phase of the wavefunction. This periodic modulation causes interference between parts of the cloud with different phases. KD diffraction is analogous to the interference of light waves incident upon a multi-slit screen, which diffracts the light, producing a characteristic pattern in the far-field.

After the atoms are split, the atoms can be accelerated to higher momentum states using Bloch oscillations or Bragg pulses. In Plotkin-Swing et. al.[8], the arms of the interferometer were accelerated with sequential Bragg pulses. A mirror pulse reverses the momenta of the arms and the acceleration/deceleration sequence is repeated. Once the atoms are overlapped, the phase of the grating they create can be measured.

The outer arms each interfere with the zero momentum arm to create two spatial gratings with periodicity $2k$. These spatial gratings move past one another at a speed $\hbar k/m$. For a time when the gratings are aligned, they create a high contrast grating. For moments when the gratings are out-of-phase, they form a low-contrast atom density. We measure how this contrast rises and falls with time by measuring the

intensity of a Bragg readout beam reflecting off of the grating using a photomultiplier tube (PMT). For a high contrast grating, a Bragg beam will reflect, just as it would off of a crystal in x-ray crystallography. When contrast is low, the beam will not coherently reflect light. The intensity of the reflected beam $S(T,t)$ oscillates at a frequency $8\omega_{rec}$:

$$S(T,t) = C(T,t)\sin^2\left(\frac{\phi_1(t)+\phi_3(t)}{2} - \phi_2\right) = C(T,t)\sin^2\left(8\omega_{rec}T + 4\omega_{rec}(t-2T) + \phi_{off}\right). \tag{1.7}$$

In Equation 1.7, t is time with $t = 0$ set as the time of the Kapitza-Dirac pulse, T is the time that the interferometer arms are reversed, and $C(T,t)$ is an envelope function centered at $t = 2T$ whose width is the coherence time of the BEC, $\frac{1}{k\delta v}$, with δv being the velocity spread of the BEC. The phases of each arm of the interferometer are labeled Φ_i: Φ_1 is the $|-2\hbar k\rangle$ arm, Φ_2 is the $|0\rangle$ arm, and Φ_3 is the $|2\hbar k\rangle$ arm. The term ϕ_{off} is a small overall offset phase.

Though we measure the rise and fall of the signal over multiple periods, we are only interested in one data point on that curve. We precisely measure the phase of the contrast signal at a time $2T$. The other points on the curve are used to precisely measure this particular phase. We vary T and measure the phase $\Phi(T)$ of S(T,t=2T). From Equation 1.7, $\Phi(T) = 8\omega_{rec}T + \phi_{off}$, and thus a linear fit of $\Phi(T)$ yields a measurement of $\omega_{rec} = \frac{\hbar k^2}{2m}$, where m is the mass of the atom.

We can increase the precision of our measurement by accelerating the moving arms of our interferometer to a maximum momentum separation of $|n\hbar k\rangle$, where n is an integer. In this case, $\Phi(T) = \frac{1}{4}n^2\omega_{rec}T + \phi_{off}$ which increases the precision of our measurement by n^2 with all other uncertainties held constant.

My group first experimentally realized the interferometer described with $n = 4$ with ^{174}Yb atoms in 2014.[7] They were able to demonstrate that this interferometer

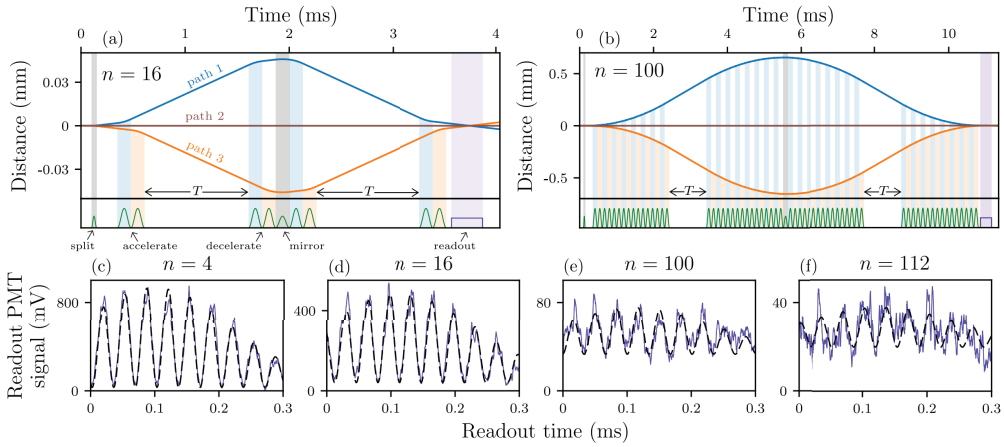

Figure 1.1 – Figure from [8]. Space time diagrams for a three-arm contrast interferometer with the arms accelerated to a momentum separation of n=16 (a) and $n = 100$ (b) with $T = 1$ for both interferometers. The intensity profile of the pulses are shown in green below each space time diagram. Pulses affecting path 1 (2) are connected to the path via blue (orange) shading and pulses affecting the momentum of both paths are shaded in gray. Each arm is accelerated sequentially. The readout light which is Bragg reflected from the final wavefunction is shown in purple. The resulting reflections are shown in (c,d) (20 shot averages) and (e,f) (80 shot averages) for different n.

is insensitive to certain effects that could diminish the quality of our signal.

The first effect is the vibrations of the mirrors involved in the light pulses. A measurement of the recoil frequency could be performed with a two-arm geometry by looking at the phase of the interference between two arms as a function of T. However, this measurement would be vulnerable to changes in the phase that are not caused by the quantum phase from the atoms' kinetic energy but rather from mirror vibrations.

Had we chosen another readout method, vibrations in mirrors reflecting that light onto the atoms would also affect the quality of our signal. In our current readout scheme, the two interferometers comprising the three arm interferometer act as rulers for one another since we are measuring the extent to which they are overlapped. If we had an external grating that we used to measure the moving gratings against, our measurement would be affected by vibrations in the mirrors sending in this external grating.

This phase insensitivity was demonstrated in by replacing the Bragg readout beam with the same Kapitza-Dirac pulse used in the beginning of the experimental sequence. As the gratings move past one another, the population diffracted into the higher momentum states oscillates at a frequency $4\omega_{rec}$. The visibility of the signal from this alternative measurement declined on the order of 1.5 ms, whereas the visibility of the signal from the CI with the Bragg readout beam was essentially unchanged over $20\,ms$.[7]

The use of a BEC increases the strength of our signal. Both the signal amplitude and coherence time increase with the use of a BEC atom source.[20]

1.7 Systematics

A systematic is an effect which shifts the measured value of a quantity from its real value. With higher precision measurements, there are more opportunities for physical effects to cause a systematic shift in that measurement. The design of our experiment was chosen to be insensitive to certain effects that could cause us to measure a value which is not α. The symmetry of the interferometer means that our signal is insensitive to any field that causes a constant shift or gradient in energy (see Equation 1.7) since this would not change with T or shot-to-shot. Our isotope of Yb has a ground state which is insensitive to magnetic fields. The overall effect of fields can be reduced or measured to below the ppb level. Finally, the contrast interferometer can be made insensitive to mirror vibrations [2].

As mentioned earlier in the chapter, a systematic which my experiment seeks to control is diffraction phases. When the BEC is in the presence of light, its phase is not evolving like a free particle. Rather, its phase is evolving at a rate corresponding to its true energy eigenstate. In the presence of a standing wave of light, this is a Bloch state. The diffraction phase is then the phase difference accrued due to the energy difference between a free particle and a band dispersion.

If this was a constant offset to all three arms of the interferometer, then our measurement wouldn't be sensitive to diffraction phases. It would only cause a constant, T-independent phase offset of our signal. However, from measurement to measurement, the intensity of the light naturally varied. In particular, the relatively long mirror pulses had a non-negligible effect on the final phase. Therefore, this

[2]With sequential Bragg pulses, our interferometer is no longer fully insensitive to vibrations. Any mirror movement between two sequential pulses on the outer arms would show up as a phase shift. However, there was no evidence to suggest that vibrations were a source of error for the interferometer in [8] because the timing between sequential Bragg pulses affecting the outer arms was small ($\simeq 130\,\mu s$) compared to vibration periods (on the order of seconds).

introduced a random phase that varied and contributed to noise in the measured phase. When this variation was taken into account, the final phase measurement had a smaller variance from shot to shot. This systematic becomes more complicated in the case of accelerating arms, which is to be discussed in latter portions of the thesis.

The other major systematic present in the interferometer is interactions. Unintentional density differentials in the three momentum states shift the phase evolution rate of each arm of the interferometer. One way to mitigate this systematic is to reduce interactions such that the shift is so small that it does not affect the final measurement. My lab has developed a technique to decrease the density of our BEC by "painting" our optical dipole trapping beams.[22], as described in Section 3.3.3. We raster the beam at a frequency much higher than the trap frequency such that the atoms "see" a time-averaged potential that spatially wider than an unrastered beam. This increases the volume of the trap while keeping the number the same, hence decreasing density.

Another approach to taking care of this systematic is to model its effect on the atoms and subtract the effect from the final phase.The effect of interactions is modeled in [23] as affecting the signal in four ways:

- Interactions shifting the phase evolution, proportional to density.
- Interactions being enhanced when clouds from different interferometer arms interacting
- A phase shift from nonzero momentum arms accelerating away from the zero momentum arm
- Accelerating branches means the interferometer might not close at the time of

the readout pulse. This effect can be mitigated at the cost of amplifying other interaction effects.

With control of interactions and diffraction phases, our goal is to measure α at the 0.05 part per billion (ppb) level in precision. To measure α beyond this precision, our limiting quantity would no longer be h/m_{Yb} but rather the ratio of the mass of ytterbium to the mass of the electron.

For a detailed analysis on systematics in our contrast interferometer relevant to measuring the fine-structure constant, see [20].

Chapter 2

BRAGG PULSES AND BLOCH OSCILLATIONS

2.1 Bragg Pulses

A traditional interferometer uses light waves that reflect off of mirrors. A particularly useful type of mirror, which is the kind used in our lab is a dielectric mirror. In a dielectric mirror, the lightwaves reflect off of layers of reflective surfaces, with separations chosen such that the light reflected from each surface constructively interferes. The essential ingredients to this process is a wave and a periodic potential. Since matter is also a wave and light can be made into a periodic potential, reflection can occur.

Bragg diffraction involves the stimulated absorption and emission of $2N_B$ photons which form a standing wave of light. The process is mediated through a virtual electronic excited state detuned in frequency from an electronic excited state $|e\rangle$, whose population remains small. In the subsequent paragraph a quantitative model for this process will be presented.[24]

In the frame where the standing wave's nodes are not moving, a particle is Bragg reflecting off of the standing wave. To quantitatively predict this phenomenon, start with two counterpropogating beams, each with electric field E_0, traveling in the x-direction, polarized along some vector $\hat{e}$:

$$\begin{aligned} \vec{E} &= E_0 \left(\sin(kx - \omega t) + \sin(kx + \omega t)\right) \hat{e} \\ \vec{E} &= 2E_0 \sin kx \cos \omega t \hat{e}. \end{aligned} \tag{2.1}$$

An atom interacts with this light through a dipole interaction:

$$\mathcal{H}_{int} = -\vec{\mu} \cdot \vec{E}, \tag{2.2}$$

where $\vec{\mu} = \langle e|e\vec{r}|g\rangle$ is the matrix element connecting the ground and excited state, e is the charge of an electron, and $\vec{r}$ is a position vector for the electron relative to the atom's nucleus. Note that the second line of Equation 2.1 demonstrates that the light forms a standing wave.

To demonstrate that this standing wave can refect an atom, we formulate the atom's Hamiltonian as a matrix, write down an ansatz solution, and solve the Schrodinger equation to obtain the time-dependent probabilities for occupying a particular momentum state.

Consider an atom moving with a momentum which is the same magnitude as a photon with momentum magnitude $p = \hbar k$. Its energy is then $E = \frac{p^2}{2m} = \frac{(\hbar k)^2}{2m}$.

The free particle time-dependent Schrodinger equation reads

$$i\hbar \frac{\partial}{\partial t} |\Psi(t)\rangle = \hat{H}| \, |\Psi(t)\rangle \, , \tag{2.3}$$

where in the position basis $\hat{H} = \frac{\hbar^2}{2m}\nabla^2 + V(\vec{r}, t)$. Since we seek free particle solutions, $V = 0$. The solutions are then of the form

$$\Psi(x, t) = \psi(x) e^{-iEt/\hbar}. \tag{2.4}$$

Since $E/\hbar$ is the angular frequency of the dynamical phase evolution, it is helpful to define $E/\hbar = \frac{\hbar k^2}{2m} \equiv \omega_{\text{rec}}$. The time-independent Schrodinger equation is

$$\frac{-\hbar^2}{2m} \frac{\partial^2 \psi(x)}{\partial x^2} = E\psi(x). \tag{2.5}$$

The solution to this differential equation is a linear combination of planewaves with wavevector $\pm k$: $\psi(x) = Ae^{ikx} + Be^{-ikx}$, where A and B are constants. The time-

dependent eigenstates are thus planewaves which can be written as:

$$\Psi(x,t) = Ae^{i(kx-\omega t)} + Be^{i(-kx-\omega t)}. \tag{2.6}$$

Since we anticipate an atom absorbing photons and thus changing its momentum in units of $2\hbar k$ by momentum conservation, we can write the eigenbasis of the free particle as the set of plane waves with wavector mk, where m is an integer. To formulate the Hamiltonian matrix, we use the free particle eigenbasis states, $|internal, external\rangle$, labeled by the internal state as either e or g for the electronic ground and excited state, respectively and the external momentum state $p = m\hbar k$.

To write down the matrix element between different momentum states consider the Hamiltonian from Equation 2.2 acting on a momentum state $|g, m\rangle$. The electric field from the standing wave in Equation 2.1 can be written as the real part of

$$\vec{E} = iE_0 \left(e^{i(kx-\omega t)} + e^{i(kx+\omega t)}\right) \hat{e}. \tag{2.7}$$

Evaluating $\langle m|\mathcal{H}_{int}|m'\rangle$ then involves evaluating $e^{i(kx\pm\omega t)} |g(e), e^{i(mkx)}\rangle = |e(g), e^{i((m\pm1)kx)}\rangle$. In this way, the electric field from the standing wave acts as a quantum mechanical operator, raising and lowering the momentum of an atom and changing its internal state. Now consider an atom with momentum $\hbar k$ in the state $|g, 1\rangle$ in the presence of a standing wave of light undergoing a single two-photon process, as shown in Figure 2.1. The interaction Hamiltonian connects adjacent states in momentum space, so we consider the final state $|e, 0\rangle$ and $|g, -1\rangle$. The interaction Hamiltonian can then be written as

$$\mathcal{H}_{int} = -ie^{-i\omega t}\hbar\Omega_R \left(|e,0\rangle \langle g,-1| - |e,0\rangle \langle g,+1|\right) + h.c. \tag{2.8}$$

where

$$\Omega_R = \frac{\mu E_0}{\hbar} \tag{2.9}$$

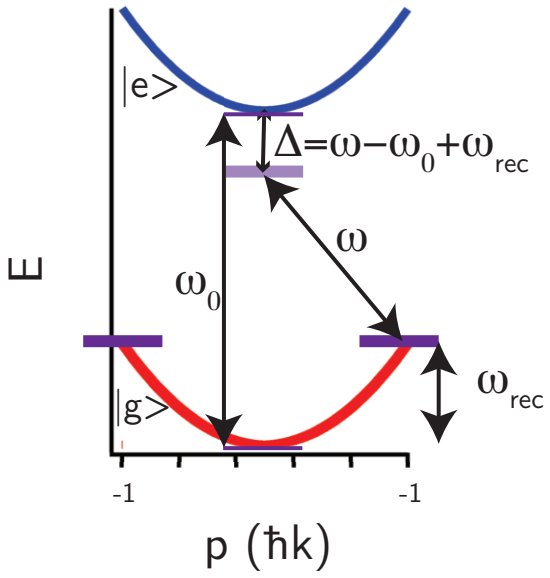

Figure 2.1 – Energy vs particle momentum diagram for the ground ($|g\rangle$, red) and excited state ($|e\rangle$, red) for a two-photon Bragg process connecting the $|g,+1\rangle$ and $|g,-1\rangle$ states, shown at $q = \pm 1$ at the purple bar. The virtual state is shown as a partially-transparent state at $q = 0$ at an energy spearation of $\Delta = \omega - \omega_0 + \omega_{\rm rec}$ from the excited state dispersion.

is the single photon Rabi frequency. The terms in the Hamiltonian listed are responsible for absorption whereas the Hermitian conjugate (h.c.) terms are responsible for stimulated emission. The full Hamiltonian in the $\{|g,1\rangle, |e,0\rangle, |-1,0\rangle\}$ basis, including diagonal terms, can be written as

$$\mathcal{H} = \begin{Bmatrix} \hbar\omega_{\rm rec} & ie^{-i\omega t}\frac{\hbar\Omega_R}{2} & 0 \\ -ie^{i\omega t}\frac{\hbar\Omega_R}{2} & \hbar\omega_0 & -ie^{-i\omega t}\frac{\hbar\Omega_R}{2} \\ 0 & ie^{i\omega t}\frac{\hbar\Omega_R}{2} & \hbar\omega_{\rm rec} \end{Bmatrix}$$

Let the ansatz solution be

$$|\Psi(t)\rangle = c_{-1}(t)e^{-i\omega_{\rm rec}t}\,|g,-1\rangle + c_0(t)e^{-i\omega_0 t} + c_{+1}e^{-i\omega_{\rm rec}t}\,|g,+1\rangle\,. \tag{2.10}$$

Plugging in $\mathcal{H}$ and the ansatz yields first-order coupled differential equations which can be solved to yield

$$\begin{aligned} c_{-1}(t) &= e^{-\frac{i}{2}\Omega_R^{(2)}t}\cos\left(\frac{\Omega_R^{(2)}t}{2}\right) \\ c_0(t) &= -i\frac{\Omega_R}{2\Delta}e^{-i\Delta t}e^{-i\Omega_R^{(2)}t} \\ c_{+1}(t) &= ie^{-\frac{i}{2}\Omega_R^{(2)}t}\sin\left(\frac{\Omega_R^{(2)}t}{2}\right), \end{aligned} \tag{2.11}$$

where $\Delta = \omega - \omega_0 + \omega_{\rm rec}$[1] , $\hbar\omega_0$ is the energy separation between the electronic ground and excited state,

$$\Omega_R^{(2)} = \frac{\Omega_R^2}{2\Delta} = \frac{\Omega_R^2}{2(\omega-\omega_0)}, \tag{2.12}$$

and the equations are solved in the limit that $|\omega - \omega_0| \gg \omega_{\rm rec}$.

The solution demonstrates that after some time t, nearly all atoms can be transferred from one momentum state to the other. Since $|c_0|^2 = \frac{\Omega_R^2}{4\Delta^2} \neq 0$, there is still a population in the excited state which can be suppressed by choosing large Δ.

Higher order Bragg pulses can be used for N_B-order processes. The generalized Rabi frequency is given by

$$\Omega_{\rm R}^{(2N_{\rm B})} = \frac{\left[\omega_{\rm R}\right]^{2N_{\rm B}}}{2^{4N_{\rm B}-3}\left[(N_{\rm B}-1)!\right]^2\Delta^{N_{\rm B}}\omega_{\rm rec}^{N_{\rm B}-1}}. \tag{2.13}$$

In this derivation it was assumed that the atoms were moving at $|p| = \hbar k$. To accelerate atoms of any speed, in the frame of the lattice, the atoms must be at a

[1]Our work in [25] demonstrates that corrections are needed for this formula due to excluding higher energy states

momentum of $\pm m\hbar k$, where m is an integer. The standing wave's velocity can be controlled by controlling the detuning between the beams and thus the detuning can be tuned to meet the Bragg condition. For atoms at rest in the lab frame, this Bragg condition reads

$$\delta = 4N_B\omega_{\text{rec}}. \tag{2.14}$$

In general, the detuning needs to chosen be such that the atoms are reflecting in the frame of the standing wave and thus the lattice momentum should be half way between the initial and desired final momentum state.

2.2 Band Structure

The first graduate student of Werner Heisenberg, Felix Bloch, pioneered fruitful models on the behavior of electrons in solids. He is responsible for the eponymous "Bloch's Theorem" on the wavefunctions of particles in periodic potentials. On developing the model described in this section, he writes[26]

> "When I started to think about it, I felt that the main problem was to explain how the electrons could sneak by all the ions in a metal to avoid a mean free path of the order of atomic distances. Such a distance was much too short to explain the observed resistances, which even demanded that the mean free path become longer and longer with decreasing temperature. But Heitler and London had already shown how electrons could jump between two atoms in a molecule to form a covalent bond, and the main difference between a molecule and a crystal was only that there were many more atoms in a periodic arrangement. To make my life easy, I began by considering wave functions in a one-dimensional periodic potential. By straight Fourier analysis, I found to my delight that the wave

> differed from a plane wave of free electron only by a periodic modulation. This was so simple that I didn't think it could be much of a discovery, but when I showed it to Heisenberg he said right away, "That's it." Well, that wasn't quite it yet, and my calculations were only completed in the summer when I wrote my thesis on "The Quantum Mechanics of Electrons in Crystal Lattices."

One could see the behavior of atoms in the presence of an optical lattice as similar to the behavior of electrons in the presence of a lattice of ion cores. As was developed by Bloch, the behavior of these electron has been traditionally understood through the lens of band structure and the same models can be applied to atoms in an optical lattice.

Examining the band structure of an atom is a tool to build language to model the behavior of particles in periodic potentials in a clear way. Mapping the band structure for a potential involves graphing the dispersion relation for a particle which is the energy as a function of momentum. It can be seen as an organized list of eigenvalues for a particular potential. For the simplest potential, $U_0 = 0$, the eigenvalues are a continuous set of numbers with the energy-momentum relationship: $E = \frac{p^2}{2m}$. The band picture is simply a parabola.

For the case of a periodic potential, Bloch's theorem dictates that the eigenfunctions are also periodic with the same spatial periodicity as the potential, a. The wave functions can all be written as $\psi = e^{ikr} \times u(r)$, where $u(r)$ has the same periodicity as the Hamiltonian and $k = 2\pi/a$, where a is the spatial period of the potential. In the case of a potential of periodicity $a \neq 0$, it is helpful to define a Brillouin zone for k: $|k| < \frac{2\pi}{a}$, from which to choose k. Choosing a k outside this range is allowed, however, one is not choosing a state that isn't already represented with a k

within the Brillouin zone. In the band picture, each eigenstate and eigenvalue can be indexed by k and band number, b.

2.3 Bloch Oscillations

Bloch oscillations generally refer to the behavior of a particle in a periodic potential experiencing a force. In our case, the periodicity and force is due to a walking optical lattice. Consider an atom in an eigenstate of a lattice potential at quasimomentum q and band b, $|b, q\rangle$. The quasimomentum of an atom is a function of the detuning δ between the beams composing the optical lattice. As the detuning is swept adiabatically, the atom will stay in an eigenstate of the Hamiltonian. When the quasimomentum is swept across the edge of the Brillouin zone and meets the adiabaticity criterion, it will stay in band b and its quasimomentum will map back into the Brillouin zone. The adiabaticity criterion reads

$$| \langle u_{b,q}| \frac{d}{dt} |u_{b',q}\rangle | \ll \frac{E_b(q) - E_{b'}(q)}{\hbar}, b \neq b', \tag{2.15}$$

where b' indexes some band other than b, $E(q)_b$ is the energy of a band b. If an atom avoids interband transitions and thus stays in a single band as its quasimomentum changes then it performs Bloch oscillations. From the frame of the lattice, the energy of the particle hasn't changed. However, since the nodes of the lattice are increasing its speed relative to the lab frame, staying in a particular band means a particle is also accelerating with respect to the lab frame, which is how Bloch oscillations are used to accelerate atoms.

Chapter 3

OUR APPARATUS AND BEC CREATION

This chapter describes the machine we use to create the ytterbium (Yb) BEC we perform our experiments on. The machine is described in detail in Ben's thesis[27] so only an overview will be given.

3.1 Ytterbium

We use ^{174}Yb for the experiments described in this thesis. It is a lanthanide element with properties similar to group II alkaline earth atoms. Its electronic structure is similar to helium which can be used to intuit its electronic behavior.

it is useful to us for a variety of reasons.

- **Magnetic Insensitivity**. Its magnetically insensitive $^1S_0$ ground state has no nuclear spin and the electronic wavefunction has a total angular momentum of zero ($J = 0$). Thus, ^{174}Yb it is effectively insensitive to magnetic fields.

- **Transitions**. Its electronic transitions allow us to cool and diffract it with commercially available lasers.

- **Blue readout**. We can Bragg reflect 399 nm light off of a grating created with our 556 nm light at a geometrically convenient angle (see Chapter 7).

- **Isotopes**. There are a variety of accessible isotopes (see Figure 3.1) which could be used to control for isotope-specific systematics for future experiments.

Isotope	Natural Abundance	Nuclear spin
^{168}Yb	0.0013	0
^{170}Yb	0.0305	0
^{171}Yb	0.143	1/2
^{172}Yb	0.219	0
^{173}Yb	0.161	5/2
^{174}Yb	0.318	0
^{176}Yb	0.127	0

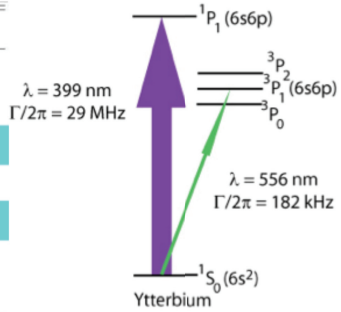

Figure 3.1 – Figure from [27]. On the left is a list of isotopes of Yb with the fermionic ones highlighted in blue. On the right is an energy diagram which includes the relevant transitions.

- **BECs** Yb can be cooled to quantum degenerate states.

In these experiments we use two transitions, as shown in Figure 3.1. The first is a broad 399 nm dipole transition from the $^1S_0$ ground state to the $^1P_1$ state. This transition is used for cooling the atoms starting from 100's of Kelvins as well as imaging.

The second transition is from the ground to the $^3P_1$ state. This intercombination transition is narrow and we use it for second-stage cooling at lower temperatures, as detailed in Section 3.3 as well as diffraction.

3.2 Apparatus

We perform our experiments in an ultrahigh vacuum chamber that fits on one 5 × 10 foot optics table with a spectroscopy set-up taking up a portion of another optics table. Figure 3.2 shows a schematic and for more details, see [27]. The machine can be organized into four sections: vacuum chamber, lasers, optics, electronics.

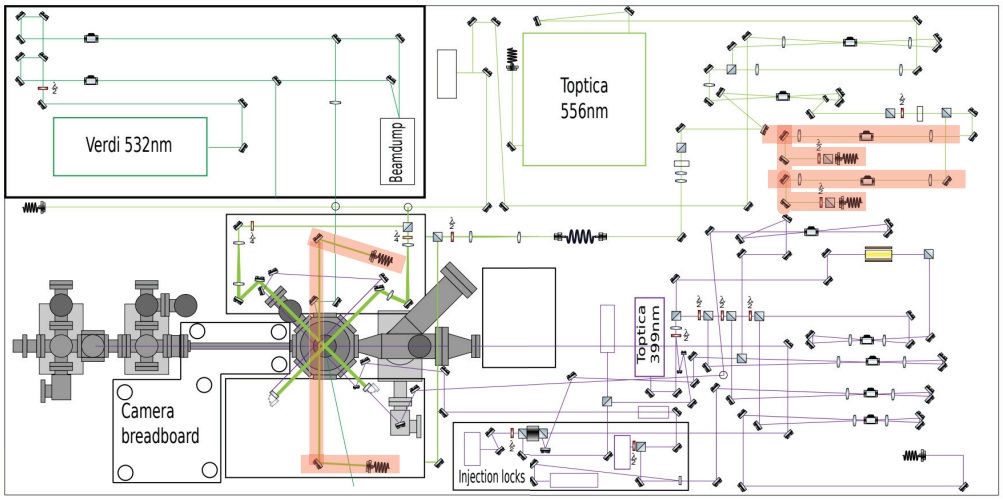

Figure 3.2 – A schematic for our optics table and lasers. The diffraction optics are highlighted in a salmon color. The diffraction light is split into two paths each going through two separate acousto-optical modulators (AOMs) in a single-pass configuration. We control the frequency shift of each AOM with a direct digital synthesizer (DDS). The light is sent through a pm fiber up to the science chamber. A polarizing beamsplitting cube follows the output of the fiber. A pick-off is obtained for intensity feedback. Figure adapted from Figure 2.8 in [27].

3.2.1 Vacuum Chamber

The chamber is maintained at pressures in the $\lessapprox 10^{-10}$ Torr and maintained with an ion pump and a titanium sublimation pump. The main components of the vacuum are an oven which contains hot Yb, a Zeeman slower, and a science chamber with 8 viewports for optical access.

3.2.2 Lasers

We have a total of five light sources: two diode lasers, two free-running diodes, and a diode-pumped laser.

- **399 nm laser** We use a Toptica DL Pro module which is an external cavity diode laser (ECDL).

- **556 nm light** We use the Toptica TA/SHA Pro laser system. It consists of a DL Pro (diode laser) which outputs IR light of about 35 mW at 1112 nm. The IR light is amplified with a tapered amplifier (TA) to about 900 mW. A second harmonic generation (SHG) cavity doubles the frequency to 556 nm. The cavity mirrors are locked to maximize output using a Pound-Drever-Hall technique.

- **Free-running Diodes** The 399 nm laser doesn't output enough power to operate our experiment so we supplement by injection locking two free-running diodes to our main 399 nm laser. Injection locking includes directing narrow-frequency 399 nm light into the relatively broadband free-running diodes. It serves the purpose of narrowing their frequency bandwidth for use in our Zeeman slower (Section 3.3.1) and cross-beam, which will not be described in this

section (details can be found in [27]). Here is a technical note on the behavior of these diodes. The slower diode tends to become misaligned with the isolator in the optical path whereas the cross-beam diode does not. I have tried to tighten the diode chip within the case which didn't seem to help. it is not yet clear what is causing this long-term drift. It seems to get worse with use of the machine.

- **532 nm laser** We use a Coherent Verdi V18 which outputs 18 W at 532 nm. One technical note for interferometeers: if you notice the power decreasing, check for damage optics. The 532 nm light has been found to damage the optics on the timescale of months, evinced by beam-sized cloudy spots on the beam path.

3.2.3 Optics

Each laser is split into multiple paths whose frequency is finely controlled for various purposes using acousto-optical modulators. Acousto-optic modulators (AOMs) work by deflecting light and shifting its frequency through a Bragg process. The AOM deflects light because a piezoelectric transducer vibrates the AOM crystal to create sound waves. In the frame of the nodes of the waves, the light is Bragg-reflecting and in the lab frame the light gets frequency-shifted and deflected.

3.2.4 Electronics

We use a computer program called Cicero for our experimental sequences which is commonly used by many ultracold atom and BEC experiments.. Through this interface we control digital and analog outputs. We use National Instruments (NI) PCIe 6535B and PCI 6713 cards to control the digital and analog signals, respectively.

The digital channels go through isolator boxes and the analog channels go through an NI BNC 2110 breakout box.

3.3 Cooling

We cool our atoms from thermal atoms (≈ 650K) to quantum degeneracy ($\approx 10^{-8}$K) through the cooling methods detailed in this section. The purpose of cooling to quantum degeneracy is to minimize the velocity width of the atom cloud to much less than a recoil velocity $v_r = \hbar k/m$.

3.3.1 Zeeman Slower

We start with Yb atoms in an oven whose nozzle is at 450° C. They exit the oven through a set of apertures which causes the atoms to form an atomic beam. The beam of atoms is slowed with a Zeeman slower with 399 nm light. A Zeeman slower uses light which propagates in the opposite direction of the atomic beam to slow the atoms down. It also contains a coil to Zeeman shift the excited state to keep the atoms in resonance with the slower beam. Without the magnetic coils, the slowing of the atoms would Doppler shift them out of resonance with the light. Currently our slower light is at a detuning of -807 MHz. An additional stage of laser cooling with 399 nm light is performed in our "crossed-beam slower." A full-description is omitted and details can be found in Section 3.1.4 in [27].

3.3.2 Magneto-Optical Trap

We use a magneto-optical trap (MOT) which uses 6 circularly-polarized beams and current-carrying coils of wire which create magnetic fields to trap and further cool our atoms. Our MOT beams start out at a -13 MHz detuning from the 556 nm tran-

sition. Once we have sufficiently loaded the MOT, we compress it by increasing the magnetic field gradient, bringing the frequency of the light closer to resonance, and turning down the intensity of the light. The CMOT generally reaches temperatures on the order of $10's$ of μK

3.3.3 Optical Dipole Trap

An optical dipole trap (ODT) is used for our final stage of cooling from thermal atoms to a Bose-Einstein Condensate (BEC). Our lab's ODT consists of two beams propagating nearly orthogonally with one vertically-oriented and one horizontally-oriented. They are sourced from our 532 nm laser. The depth of the potential due to an ODT is given by[1]

$$U_0 \approx \frac{\hbar\Omega_R^2}{4\Delta} = \frac{\hbar\Gamma^2 I}{8\Delta I_{sat}}, \tag{3.1}$$

where Ω_R is the Rabi frequency defined in Equation 2.9, Δ is the detuning of the light from a particular transition, Γ is a linewidth of the transition in units of angular frequency, I is the intensity of the light, and I_{sat} is the saturation intensity of the transition.

In our ODT, both the 556 nm and 399 nm transitions contribute to the total potential from the ODT light. Owing to the ratio of Γ^2/Δ for each transition, the magnitude of the potential from the 556 nm transition is about 10% of the contribution from the 399 nm transition. The potential due to the 399 nm transition is negative ($\omega - \omega_0 < 0$) and is responsible for trapping the atoms. On the other hand, the potential due to the 556 nm transition is positive and therefore decreases the depth of the trap for a given power.

---

[1] In the limit that $|\delta| \gg \Omega$ and $|\delta| \gg \Gamma$

3.3.4 Classical Derivation of Optical Dipole Behavior

The qualitative behavior of an optical dipole trap can be predicted by considering the atom as a polarizable object in an electric field.

The interaction energy of a dipole with an applied field is given by

$$U = -\frac{1}{2}\epsilon_0 \chi_{\mathrm{a}} E^2 = \frac{1}{2} e\mathbf{r} \cdot \mathbf{E}, \tag{3.2}$$

where $\epsilon_0 \chi_{\mathrm{a}}$ is the scalar polarizability, $\vec{E}$ is the electric field, $e\vec{r}$ is the induced dipole moment.

Let an electric field $\vec{E} = E_0 \cos(\omega t - kz)\widehat{\mathbf{e}}_x$ due to the ODT light be applied to the dipole. The force in the z-direction is given by

$$F_z = -ex \left\{ \frac{\partial E_0}{\partial z} \cos(\omega t - kz) + kE_0 \sin(\omega t - kz) \right\}. \tag{3.3}$$

Modeling the electron as a harmonic oscillator, we can write its position x as $x = \mathcal{U}\cos(\omega t - kz) - \mathcal{V}\sin(\omega t - kz)$, where $\mathcal{U}$ and $\mathcal{V}$ represent the in phase and quadrature to the applied field, respectively. The force then becomes

$$\begin{aligned} F_z = -e\{&\mathcal{U}\cos(\omega t - kz) - \mathcal{V}\sin(\omega t - kz)\} \\ &\times \left\{ \frac{\partial E_0}{\partial z} \cos(\omega t - kz) + E_0 k \sin(\omega t - kz) \right\}. \end{aligned} \tag{3.4}$$

To solve for $\mathcal{U}$ and $\mathcal{V}$, one can solve the damped harmonic oscillator equation of motion

$$\ddot{x} + \beta \dot{x} + \omega_0^2 x = \frac{F(t)}{m} \cos \omega t, \tag{3.5}$$

where β is a friction coefficient defined by $F_{friction} = m\beta\dot{x}$, and ω_0 is the natural frequency of oscillation for the electron. Under the assumption that $\mathcal{U}$ and $\mathcal{V}$ change

slowly with respect to ω (the slowly-varying envelope approximation), the final form of $\mathcal{U}$ and $\mathcal{V}$ is

$$\begin{aligned} \mathcal{U} &= \frac{\omega_0 - \omega}{(\omega - \omega_0)^2 + (\beta/2)^2} \frac{F}{2m\omega} \\ \mathcal{V} &= \frac{-\beta/2}{(\omega - \omega_0)^2 + (\beta/2)^2} \frac{F}{2m\omega} \end{aligned} . \tag{3.6}$$

After time-averaging over many oscillation cycles, using $I = \frac{1}{2}\epsilon_0 c E_0^2$, repeating the derivation in the x- and y-direction, and plugging in Equations 3.6 into Equation 3.4, the final average radiation force, as predicted classically, can be written as

$$\overline{\mathbf{F}} = \frac{e^2}{2\epsilon_0 mc} \left\{ \frac{-(\omega - \omega_0)}{(\omega - \omega_0)^2 + (\beta/2)^2} \frac{\nabla I}{\omega} + \frac{\beta/2}{(\omega - \omega_0)^2 + (\beta/2)^2} \frac{I}{c} \frac{\mathrm{k}}{|\mathbf{k}|} \right\} \tag{3.7}$$

. The first term in Equation 3.3.4 shows that the force is proportional to the gradient of the intensity ∇I and the force is attractive in the direction of higher intensity in the case of red detuning ($\omega < \omega_0$). In the limit of $\Delta >> \Gamma(\beta)$, the denominator of the first term results in the $1/\Delta$ factor found in Equation 3.1. The second term which arises from absorption is proportional to the intensity and is in the direction of k.

3.3.5 Evaporation

To evaporatively cool the atoms, the ODT depth is lowered such that the hottest atoms preferentially evaporate. The trap depth is lowered by decreasing the power in the ODT beams. Important to creating large BEC's, we "paint" our horizontal ODT beam[22] such that its center's position oscillates quickly in space at some frequency f_{paint} as seen in Figure 3.3. By controlling the relationship between position and time, we can paint potential landscapes. This relies on the fact that if we paint fast

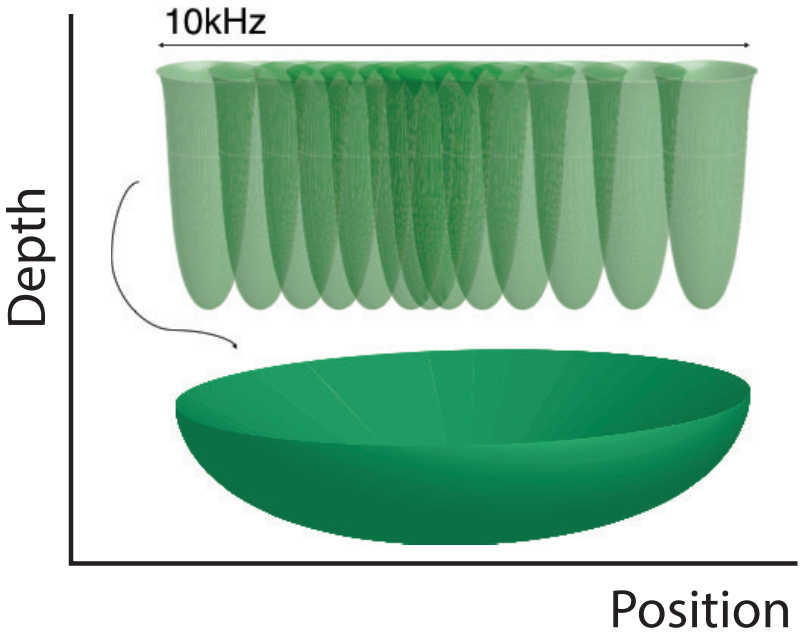

Figure 3.3 – Schematic for painting. The upper figure shows spatial profiles at equal time intervals as it is rasterized. The time-averaged potential is shown in the bottom graph. Because the beam spends more time in the center, the time-averaged potential is larger there.

enough, particularly much faster than trap frequency f_{trap} ($f_{paint} \gg f_{trap}$), the atom "sees" a time-averaged potential.

In the evaporation sequence, we use painting in the beginning when it is loaded from the compressed MOT to create a large volume trap. We employ it again at the end of evaporation to again increase the size of the ODT to reduce interactions. As repulsive interactions lead to an increased velocity width, reducing the density and thus interactions is important for phase coherence across the cloud. Phase space density is given by

$$\rho = n\lambda_{dB}^3, \tag{3.8}$$

where n is the number density and $\lambda_{dB} = h/p$, where p is the momentum of an atom and h is Planck's constant. When $\rho \approx 2.6$, the transition to BEC occurs.

Through our cooling sequence, we generally end with $\simeq 10^5$ condensed atoms.

3.4 Diffraction Beams

This section will describe the diffraction beam experimental details for the experiments described in subsequent chapters unless noted otherwise. Our difraction beams are sourced from the same laser that generates our MOT light. The optics set-up is shown in Figure 3.2.

In general the spatially dependent depth of an optical lattice is given by

$$U_0 = \frac{\hbar\Omega_R^2}{\Delta}\cos^2(kx), \tag{3.9}$$

where Ω_R is the single-beam Rabi frequency. Note that the peak depth is larger than the depth of an ODT (Equation 3.1) by a factor of 4. This is because the maximum intensity of a standing wave made with two beams is 4 times greater than the maximum intensity of a single beam (see Section 5.6.1).

Two different detunings from resonance with the ${}^1S_0 \rightarrow {}^3P_1$ are used: $\Delta = 3500\Gamma$ and $\Delta = 1300\Gamma$, where $\Gamma = 2\pi \times 182\,\text{kHz}$. The lower detuning is used to increase the depth of our optical lattices given a fixed amount of power in our diffraction beams. From Equation 3.9, it is evident that the depth can be increased by decreasing Δ.

The waist of the beams is 1.8 mm, set by the collimating optics on the fiber output. The pulses used are characterized by rise and fall $1/e$ times of $\simeq 30\,\mu$s.[25].

Chapter 4

BLOCH-BAND PICTURE FOR ATOM OPTICS

4.1 Motivation

To summarize earlier chapters, in atom interferometry we manipulate the momentum of our atoms with walking standing waves of light whose nodes are either moving at a constant velocity (Bragg pulses) or a changing velocity (Bloch oscillation pulses). Often in atom interferometry, we are motivated to increase the energy of the atoms in order to increase the phase accumulation rate, allowing for more overall phase Φ to accumulate. The more phase accumulated, the lower the uncertainty $\delta\phi/\Phi$ for a constant uncertainty in the measured CI signal phase $\delta\phi$. In addition to increasing the momentum of the atoms in even units of $\hbar k$, the light changes the internal energy of the atoms during the pulse due to the dipole interaction energy. Such altered energy means that the atoms are accumulating phase at a slightly different rate while in the presence of light. This phase shift is called a diffraction phase.

Many atom interferometry research groups contend with diffraction phases and they can constitute a technical challenge for observing a stable phase in an interferometer. In our lab, diffraction beam intensity fluctuations, even at the single digit percent level, can make the interferometer phase significantly fluctuate from shot to shot, thus precluding a repeatable experiment for certain pulses.

The band picture provides a simple and intuitive way to calculate diffraction phases and is widely applicable to most atom interferometry schemes. Using the band picture to predict these phase shifts opened our eyes to the benefits of excited-

band Bloch oscillations, which is detailed in Chapter 5. Note that that all the physics detailed in the following chapters is single-particle physics.

4.2 Atom Optics through the Lens of Band Structure

To understand the behavior of a particle in a periodic potential of depth U_0 through the lens of band structure, as described above, we first numerically solve the Shrodinger equation to obtain the potential's eigenvalues, enabling us to map the band structure. Once this picture is obtained, the energy and thus phase properties of our atomic wavefunction in the presence of standing waves of light can be determined.

The potential energy created by a standing wave of light takes the form $U(x) = U_0 \cos^2(kx)$. To write the Hamiltonian's matrix, let the basis be the eigenbasis of the free particle, planewave momentum states with wave number mk for planewaves of momenta $m\hbar k$, where m is an integer. Let each free state basis state be denoted $|m\rangle$. As argued in [28], the Hamiltonian matrix has the diagonal elements given by $\langle m|H|m\rangle = (q-2m)^2 + U_0/2$ and off-diagonal elements are given by $\langle m|H|m \pm 1\rangle = U_0/4$. The set of eigenstates is infinite but can be truncated to include only states such that $|m| < \mathcal{N}$. For $\mathcal{N} = 2$, the corresponding Hamiltonian matrix is:

$$H = \begin{bmatrix} (q+4)^2 + U_0/2 & U_0/4 & 0 & 0 & 0 \\ U_0/4 & (q+2)^2 + U_0/2 & U_0/4 & 0 & 0 \\ 0 & U_0/4 & (q)^2 + U_0/2 & U_0/4 & 0 \\ 0 & 0 & U_0/4 & (q-2)^2 + U_0/2 & U_0/4 \\ 0 & 0 & 0 & U_0/4 & (q-4)^2 + U_0/2 \end{bmatrix}$$

Band structure can be found numerically by diagonalizing H. A computer program, such as IGOR or Mathematica, can take this matrix and return eigenvalues and eigenvectors to make graphs like those in Figure 4.1.

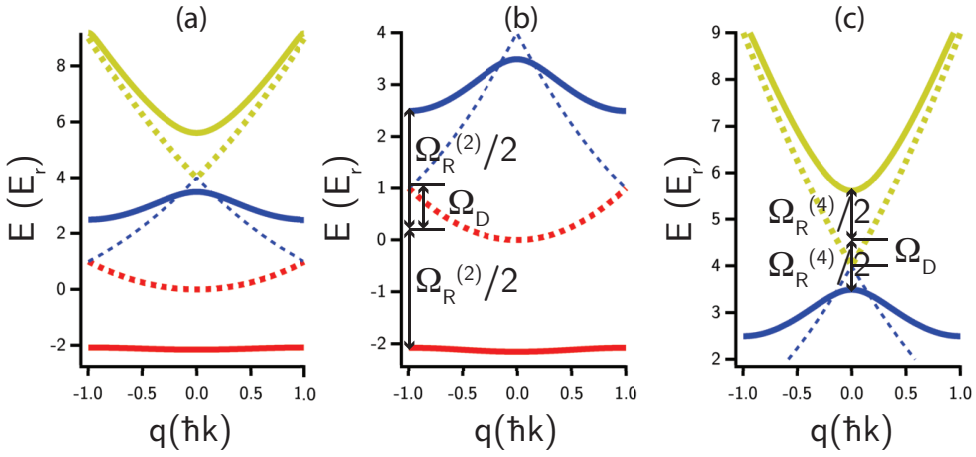

Figure 4.1 – (a) The band structure for the ground band (red), first excited band (blue), second excited band (orange) at a lattice depth of $U_0 = 10E_r$. The bands were calculated with 51 states from $|-50\hbar k\rangle$ to $|50\hbar k\rangle$ in steps of $2\hbar k$. The free space parabolic band structure for each band is shown as dotted lines. (b) A close-up graph of the band gap between the ground and first excited band. The Rabi frequency Ω_R for a first-order Bragg process is shown and the diffraction frequency of phase evolution Ω_D are labeled. The graph in (c) is the same as (b) but illustrating the first and second excited band and for a second-order Bragg pulse.

The following subsections detail how the band picture can be used to make predictions for Bragg and Bloch oscillation pulses. For more details, I direct the reader to Gochnauer et al.[25].

4.2.1 Bragg diffraction

In Chapter 1, Bragg pulses were described as a $2N_B$-photon process where a particle coherently reflects off a standing wave of light. In the band picture, this process is described with different language. When applying a Bragg pulse, a particle is loaded into the lattice at a degeneracy for a free particle, either at the band center ($q = 0$) or band edge ($q = \pm 1\hbar k$) for the two originally-degenerate bands, N_B and $(N_B - 1)$. As the lattice is adiabatically[1] turned on, the degeneracy is broken and second-order perturbation theory dictates that the two levels will repel one another, such that the particle is in an equal superposition state of the N_B and $(N_B - 1)$ bands. Because the atom is in a superposition of multiple eigenstates, it oscillates between the two bands at a Rabi frequency $\Omega_R^{(2N_B)}$, which is the energy separation between the two states divided by $\hbar$. Reflection will occur when $\int \Omega_R^{(2N_B)}(t)dt = \pi$, corresponding to when the wavefunction is in the opposite symmetry eigenstate.

The band picture can determine the diffraction phase due to this Bragg pulse. The difference between the midpoint of the repelling bands and the non-peterturbed crossing, as shown in Figure 4.1 gives the diffraction energy $\Omega_D^{(2N_B)}$. The total resulting phase shift can then be found by simply evaluating $\int \Omega_D^{(2N_B)}(t)dt$ over the duration of the pulse. To intuit this phase shift, consider that an atom spends an equal amount of time in each band[2], and so its average energy is the average of the

[1] Adiabatically with respect to the states not involved in the Rabi oscillation.

[2] This is true for a resonant Bragg pulse, i.e. when the atom is loaded at $q = 0, \pm 1$ where there initially is a degeneracy.

two band states. The average of the two band states has an energy separation of $\hbar\Omega_D$ from the crossing of the unperturbed sates. A diffraction phase difference between momentum states in an interferometer can cause a phase difference between them to accumulate which can affect the interferometer signal.

For example, consider first-order Bragg diffraction ($N_B = 1$) for an atom at rest in the lab frame, as portrayed in Figure 4.1(b). Let the detuning of the beams be set to $\delta = 4\omega_{\text{rec}}$ to meet the Bragg condition (Equation 2.14) such that the atoms are at a momentum of $q = 1\hbar k$. The lattice is then adiabatically ramped on which puts the atom in an equal superposition of the ground and first excited band at $q = 1\hbar k$. Using the notation of the lattice eigenstates as $|q, band\rangle$, and the wavefunction as $|\psi(t)\rangle = \frac{1}{\sqrt{2}}(|1,0\rangle - e^{-i\Omega_R^{(2)}(t)t}|1,1\rangle)$, reflection will occur when it has the wavefunction has evolved such that $\int \Omega_R^{(2)}(t)dt = \pi$ to the opposite parity eigenstate: $|\psi\rangle = \frac{1}{\sqrt{2}}(|1,0\rangle + |1,1\rangle)$.

The diffraction phase is found by integrating the time-dependent energy separation between the average of the two bands from the energy degeneracy, $\phi_D = \int_{pulse} \Omega_D dt$, as seen in Figure 4.1.

4.2.2 Bloch Oscillations

Chapter 1 described Bloch oscillations as the coherent reflection off of a lattice moving at a changing velocity. In this section, we will describe Bloch oscillations in the band picture. First, the atom is loaded at some quasimomentum away from band gaps such that when the lattice reaches its peak depth, the particle is in an eigenstate of the lattice potential. As the lattice is accelerated, in the atom's frame, this corresponds to the quasimomentum sweeping across the Brillouin zone.

Once the quasimomentum reaches an anti-crossing, the atom has the opportunity

to either tunnel to a different band or stay in the same band. The probability of tunneling to a higher band given in the Landau-Zener model is[29][30]

$$P_{LZ} = exp\left(-\pi\frac{\Omega_{BG}^2}{4bka}\right), \tag{4.1}$$

where Ω_{BG} is the band gap at an avoided crossing, $a = \dot{\delta}/2k$ is the atom's acceleration in the lab frame, b is the larger band number of the two bands involved in the tunneling process. For example, for an atom traveling in the first excited band traversing the $q = 0$ avoided crossing, to determine the probability of Landau-Zener tunneling, $b = 2$ should be used in Equation 4.1. When the atom crosses the avoided crossing at $q = \pm 1\hbar k$ with the ground band, $b = 1$ should be used. P_{LZ} increases both when other bands are at nearby energies or the quasimomentum is swept quickly. In order to accelerate the atoms efficiently, P_{LZ} must be small.

To keep the efficiency high and the time a wavefunction takes to traverse one Brillouin zone, T_{BO} small, a common strategy is to use a high depth lattice. However, with a high depth lattice generally comes large lattice-induced phase fluctuations that can preclude a phase-stable interferometer.

The lattice-induced phase shift is the area between the lattice energy $E_L(q(t))$ and the free space energy $E_{FS}(q(t))$. It is found by integrating the lattice-induced phase shift with respect to time:

$$\phi = \int \frac{E_L(q(t)) - E_{FS}(q(t))}{\hbar} dt = \int \frac{E_D(t)}{\hbar} dt. \tag{4.2}$$

For a linear ramp, which is typically used, this amounts to finding the area between the lattice energy band and the free space energy dispersion, as shown in Figure 4.2 and multiplying by the inverse ramp rate, $\left(\frac{dq}{dt}\right)^{-1}$.

The diffraction phase can be written in terms of an atom's energy in a lattice

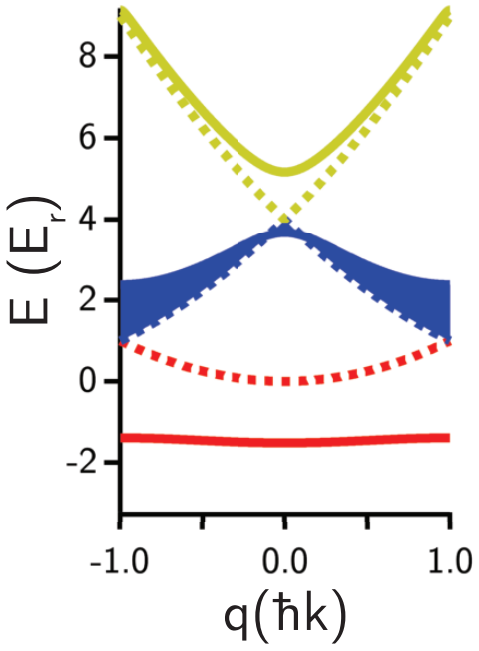

Figure 4.2 – Band dispersion (solid lines) for a lattice with $U_0 = 8E_r$. The free space energies are shown as dotted lines. The shaded area is proportional to the lattice-induced phase shift due to one BO performed in the first excited band. The bands were calculated with 51 states from $|-50\hbar k\rangle$ to $|50\hbar k\rangle$ in steps of $2\hbar k$.

averaged over one Brillouin zone, $\langle E(q(t))\rangle$:

$$\langle E_D(q(t))\rangle = \frac{1}{T_{BO}} \int \frac{E_D(q(t))}{\hbar} dt. \tag{4.3}$$

Thus,

$$\phi_D = \langle E_D(q(t))\rangle T_{BO}. \tag{4.4}$$

4.3 Bragg vs Bloch

Atoms can be accelerated with either a constant velocity (Bragg) or accelerating (BO) lattice. Both methods offer benefits but each have drawbacks. Bragg diffraction involves accelerating atoms with a constant velocity walking wave. The walking wave must be at the proper speed in the frame of the atoms to meet the Bragg reflection condition. This restriction brings us to our first drawback for Bragg pulses: you can never approach reflecting 100% of the atoms by tuning pulse parameters. This is because the atomic cloud, though at a temperature typically around 10s of nanoKelvins, has some finite velocity distribution. Even though we are able to reflect at the seemingly-high efficiency of 98.45 % per $\hbar k$ with third order pulses[8], enough of these pulses will drive the overall efficiency down and this ultimately limits the number of atoms surviving this process.

The velocity selectivity of the pulse is a function of the pulse timing. The frequency width Δf of light is inversely proportional to the pulse length Δt. To allow for a larger range of velocities, the pulse length could be shortened. However, shorter pulses can violate the Bragg adiabaticity criterion ($\delta t \gg \frac{1}{4N_B\omega_{\text{rec}}}$) and cause undesired momentum states to have a significant population.

To overcome this finite-efficiency challenge, one can use an accelerating lattice. In principle, one can make this acceleration process arbitrarily efficient. By sweeping over different velocities, the lattice is able to reflect each momentum group. It

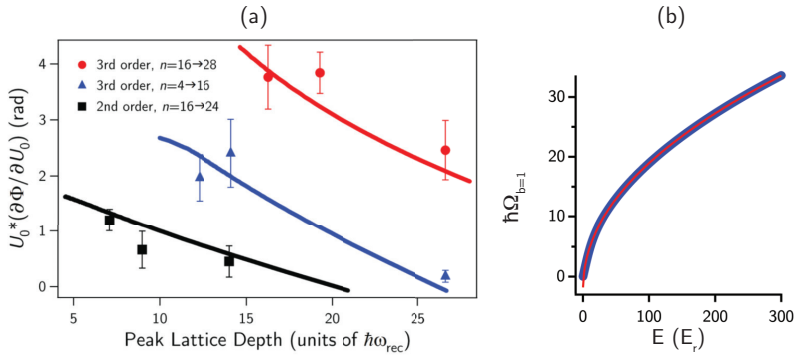

Figure 4.3 – The phase fluctuation range can be estimated using $U_0 * \frac{\partial \phi}{\partial U_0}$, plotted in (a) for various Bragg mirror pulses with Bloch-bands calculation in solid lines. (a) is taken from [25]. The initial and final values of n indicate the momentum separation before and after the pulse in units of $\hbar k$. In (b) the band gap between the first excited and bottom band is plotted as a function of U_0 (blue). A best fit power law function (red) returns that $\Omega \propto U_0^{0.5}$.

seems then that Bloch oscillations are the way to go. If so, why did we and so many other groups use Bragg diffraction in their interferometers? The issue with Bloch oscillations is that they often suffer more from lattice-induced phase shift fluctuations.

Next we will demonstrate that an interferometer which uses ground-band Bloch oscillations is more sensitive to lattice-induced phase shifts than one which uses Bragg pulses. To characterize the first-order effects of diffraction phase fluctuations, the expected phase fluctuation can be calculated as $\Delta\phi \propto \frac{d\phi_D}{dU_0} U_0$. We can calculate $\frac{d\phi_D}{dU_0} U_0$ for our third-order Bragg pulses with band structure as described in Section 4.2.1. As a function of pulse timing for a π-pulse, the relationship plotted in Figure 4.3 is obtained for various pulses connecting different momentum states.

To estimate the phase fluctuation, assume depth fluctuations are some fraction β of the depth, U_0: $\Delta U = U_0\beta$. The phase fluctuation is then approximated by

$$\Delta\phi = \frac{\partial\phi_{D,Bragg}}{\partial U_0}U_0(\beta). \tag{4.5}$$

Similarly, using also Equation 4.4, the phase fluctuation for a BO can be approximated:

$$\Delta\phi = \frac{d\phi_{D,BO}}{dU_0}U_0(.02) = \frac{\langle E_D(q(t))\rangle T_{BO}}{dU_0}U_0(\beta). \tag{4.6}$$

For Bragg pulses, the diffraction phase first derivative approaches zero for high pulse depths, but for increasing pulse depths, the adiabaticity requirement becomes more and more difficult to maintain. For increasingly short pulses, undesired momentum states become populated. Using the data point with a minimal $\frac{d\phi_D}{dU_0} \times U_0$ (third order, $U_0 = 26.6E_r$) and an estimate of a depth fluctuations as $\beta = 2\%$ of U_0, the phase fluctuations can be approximated to first-order as 4 mrad.

Compare the behavior of Bragg pulses to a ground-band Bloch oscillation. When we initially tested BOs, we used $U_0 = 45\hbar\omega_{\text{rec}}$ and $T_{BO} = 8\,\mu$s. For these parameters and assuming $\beta = .02$, $\Delta\phi \approx 71$ mrad for one BO, an increase by more than a factor of 10.

One can ask if there is another set of parameters which would produce a smaller phase fluctuation. For a smaller depth, for example, T_{BO} would have to be longer if the efficiency is to be kept the same, as determined by Equation 4.1 where exponential argument $-\pi\frac{\Omega^2}{4bka}$ should thus not change. The band gap Ω is a square root function with respect to U_0, as shown in Figure 4.3(b). Thus, if U_0 were decreased by a factor of α, T_{BO} would need to be increased by a factor of α. Using Equation 4.4, this would keep $\Delta\phi$ constant and thus using lower depths and larger T_{BO} would not yield

a smaller phase range.[3]

4.4 Excited State Bloch Oscillations

One might ask, is this phase unstable behavior true for bands other than the ground band? It turns out that the ground band exhibits unique behavior and there's more to be explored with the higher bands. We will first explore these differences.

At first glance, excited band BOs could be considered unattractive. In an excited band BO, as the quasimomentum is swept, the particle must traverse not one but two band gaps, meaning there are two chances for Landau-Zener tunneling. Moreover, these band gaps are always smaller for increasing band number for a fixed depth, meaning that it could be more challenging to keep the atom in the same band and thus efficiently and quickly accelerate. [4]Recall that changing band number through Landau-Zener tunneling means not accelerating in the lab frame.

Despite these disadvantages from the band gaps, we looked more closely at them because in the process of exploring our Bloch-bands diffraction phase calculations, we found a peculiar feature unique to excited bands. Recall that the area between a lattice band and free space band is proportional to the phase accrued during a Bloch oscillation. Consider the behavior of the area when the depth is swept from $8E_R$ to $10E_R$, as shown in Figure 4.4.

The area changes shape, but the actual area remains the same. This means that it is first-order insensitive to phase fluctuations, evading the kryptonite of Bloch oscillations. We call these depths "magic depths", which is the topic of the next

---

[3]This assumes that for the ground band, $|\langle E_D \rangle| \propto U_0$ which is approximately the case (See Figure 4.5).

[4]To possibly avoid confusion here is a spoiler: the band gap at the magic depth actually increases, as seen in Figure 5.6.

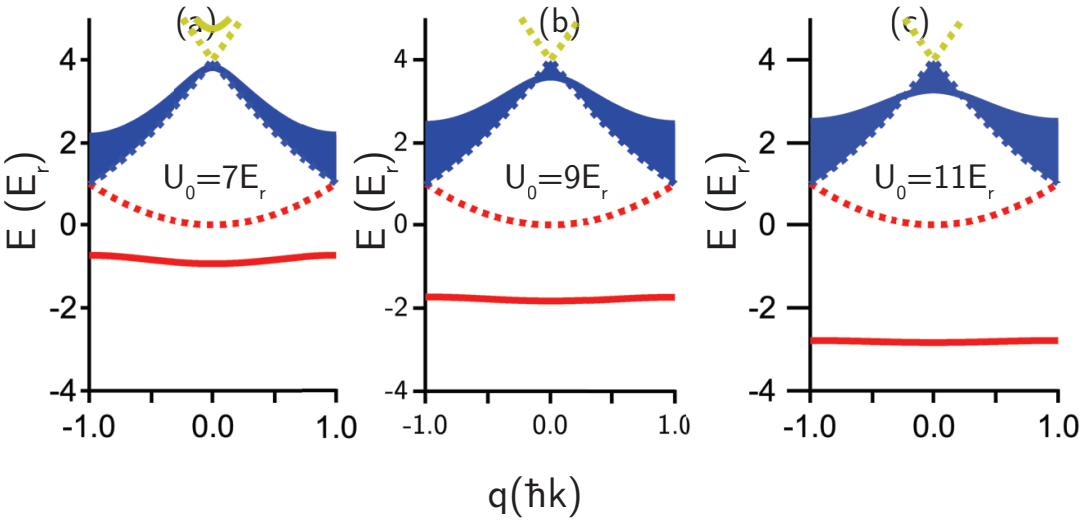

Figure 4.4 – Band structure for (a) $U_0 = 8E_r$, (b) $U_0 = 9E_r$, and (c) $U_0 = 10E_r$ with all three shown in a close-up on (d). The phase accrued during a Bloch oscillation is proportional to the shaded region. The first derivative of the area between the lattice band and free space band (shaded) vanishes as the band "flops".

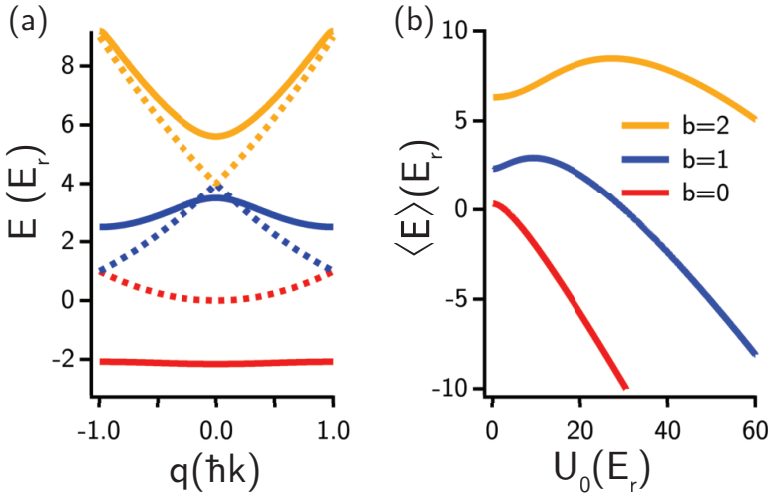

Figure 4.5 – (a) Band structue for a representative depth of $U_0 = 10E_r$. (b) The average energy for the ground band and first excited band (b=0, 1, 2) as a funtion of the lattice depth U_0. The ground band exhibits only monotonic behavior in $\langle E \rangle$ while the excited bands have local maxima.

chapter. Indeed, this feature is unique to excited band Bloch oscillations, as seen by plotting the average energy $\langle E \rangle$ as a function of the lattice depth U_0, shown in Figure 4.5(b).

Before diving into our magic depth studies, we will first compare and contrast the behavior of atoms undergoing Bloch oscillations in ground and excited band BOs. We apply BO by loading atoms adiabatically into a particular band and quasimomentum of our optical lattice. We then sweep the relative frequency detuning δ between our diffraction beams which creates an accelerating lattice in the lab frame. In the band picture, the atom is sweeping through different quasimomentum values, as seen in Figure 4.6(a).

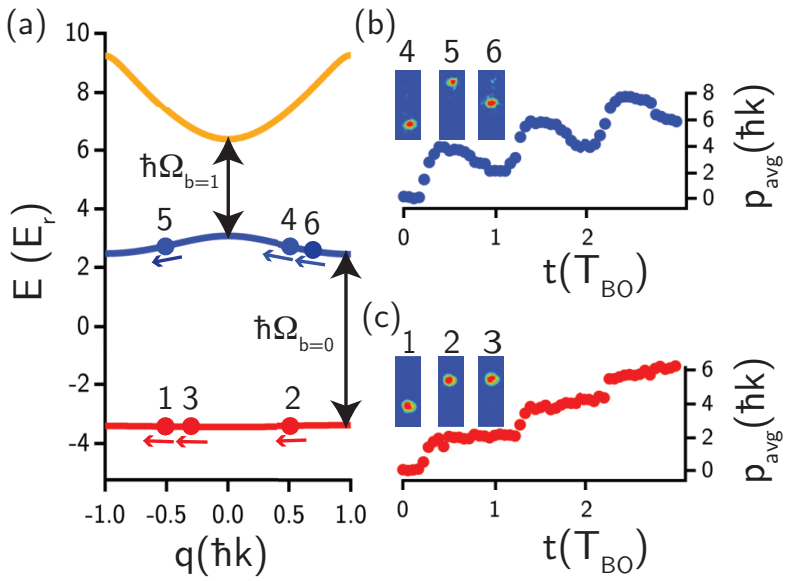

Figure 4.6 – (a) The trajectories for a particle undergoing BO in the ground (red) and first excited band (blue) for a sinusoidal potential with a depth of $U_0 = 13.6E_r$. In each case, the atom is loaded into each band at $q = 0.5\hbar k$ (away from band gaps) and the detuning between the two beams is increased. For the ground band it is loaded at (1), and it first traverses an avoided acrossing at $q = 1\hbar k$, where its momentum increases by $2\hbar k$. It then continues traveling in the ground band, keeping a constant momentum through (2) and (3). In the first excited band, the particle is loaded at (4) and first traverses the band gap with the second excited band at $q = 0$, gaining $4\hbar k$ in momentum (5). As the diffraction beam detuning is further increased, it traverses the band gap at $q = -1\hbar k$ and loses $2\hbar k$ in momentum, leaving it with a net increase of $2\hbar k$ in momentum at (6). The band gap for the two avoided crossings are labeled:$(\hbar\Omega)_{b=0}$ and $(\hbar\Omega)_{b=1}$. (b) The average lab frame momentum of the atom after it is unloaded as a function of time in units of the Bloch period T_{BO}. Absorption images corresponding to points 1-6 on (a). For this experiment, Δ/Γ=3500 and $\dot{\delta} = 2\pi \times 83kHz/\text{msec}$. The intensity ramp times are 300 μs and 600 μs for (b) and (c), respectively.

When a particle traverses a band gap (see Figure 4.7), $\frac{\partial E}{\partial q}$ changes sign and the particle changes its momentum by $2b\hbar k$, where b is the greater of the two bands involved in the band gap. A particle increases (decreases) its momenum when it starts from a q with a negative (positive) slope and ends at a q with a positive (negative) slope.

Given that to successfully perform BOs, the goal is to maximize the momentum change, one disappointing feature is that the total change inthe lab-frame momentum's magnitude is $2(b+1)\hbar k - 2b\hbar k = 2\hbar k$ for one BO period- constant for all b. The change in momentum increases with band number so it is possible that one could load to a higher band and sweep over a band gap without traversing the entire Brillouin zone. However, the lattice would still need to be loaded and unloaded in that case, which would present a challenge to maximizing momentum change in the least amount of time.

To test these ideas for the ground and first excited band experimentally, we performed Bloch oscillations while stopping at various quasimomenta corresponding to different BO times (t) and measured the free space momentum.

The atoms were adiabatically loaded into the ground band of the lattice by linearly increasing the depth from $U_0 = 0$ to $U_0 = 13.6E_r$ for $600\,\mu$s for the ground band and $300\,\mu$s for the first excited band. We loaded them at a quasimomentum of $q = 0.5\hbar k$ with a corresponding initial detuning of the beams of $\delta = 2\omega_{\text{rec}}$. We chose this quasimomentum in order to be away from band gaps to minimize the opportunities for tunneling to higher bands during the lattice loading. The relative detuning of the diffraction beams was increased at a rate of $\dot{\delta} = 2\pi \times 83\,kHz/\text{msec}$ for a varying duration corresponding to different quasimomenta. The atoms were then adiabatically unloaded for the same time at which they were loaded. The final momentum population was measured using our usual time-of-flight absorption

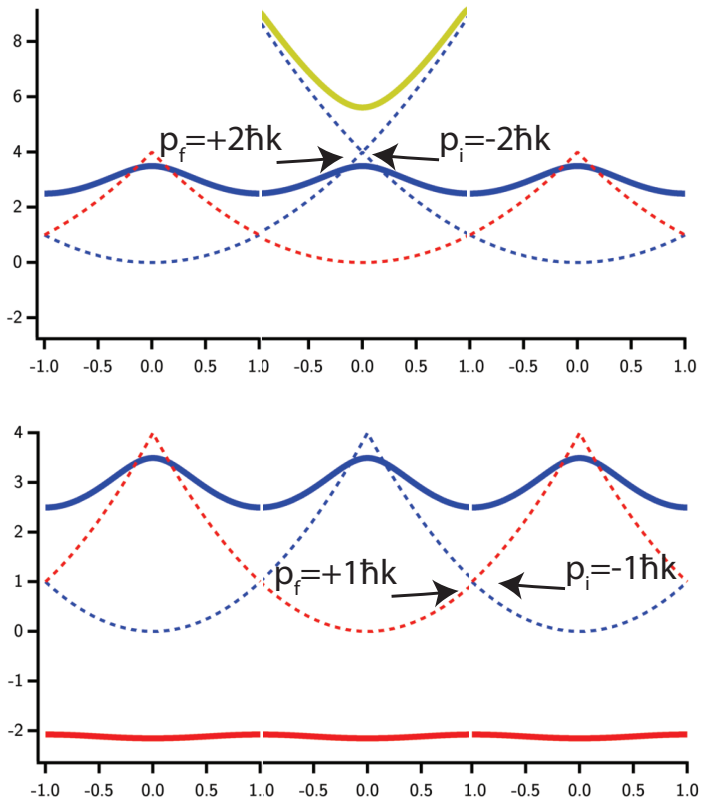

Figure 4.7 – The relevant free space momentum states used to determine the momentum change a particle undergoes when traversing a band gap. Solid lines are the band energies and dotted lines are the free particle energy states. The top graph demonstrates a momentum change of magnitude $\Delta p = 2\hbar k - (-2\hbar k) = 4\hbar k$ across the band gap between the first and second excited band. The bottom demonstrates a momentum change of $\Delta p = \hbar k - (-\hbar k) = 2\hbar k$

imaging and the average momentum was computed and is shown in Figure 4.6.

Chapter 5

MAGIC DEPTHS

This chapter will discuss the experiments we performed to observe the magic depth property in excited-band Bloch oscillations.

5.1 Depth Calibration

This section will describe how we relate the power of the diffraction beams, P, to the depth experienced by the atom, U_0. A particular power produces a Rabi frequency Ω_R and U_0 and Ω_R are related by Equation 3.9. However we perform a calibration measurement because it is unknown exactly where in the beam the atoms are. There are two methods that we have used to calibrate the beam: the Kapitza-Dirac and the Rabi method. For the Kapitza-Dirac method we split the atomic wavefunction with a Kapitza-Dirac pulse and measure the diffracted population as a function of the power. For the Rabi method we measure the Rabi frequency of population oscillation due to a Bragg pulse.

5.1.1 Kapitza-Dirac Method

A Kapitza-Dirac (KD) pulse is a short pulse characterized by a duration τ such that $\tau \ll 1/\omega_{\text{rec}}$. The pulse spatially modulates the phase and results in a momentum

distribution which is a function of the N^{th} Bessel function J_N of the first kind:

$$\begin{aligned} P_N &= J_N^2(\theta), \quad N = 0, \pm 1, \pm 2, \ldots, \quad \text{where} \\ \theta &= \int_{Pulse} \frac{\Omega_{\mathrm{R}}^2(t)}{2(\omega - \omega_0)} dt \end{aligned} \tag{5.1}$$

is the pulse area.[31][21] I recommend [24] for more details. We can write θ in terms of U_0 through Equation 3.9:

$$\frac{U_0}{\omega_{\mathrm{rec}}} = \frac{\Omega_{\mathrm{R}}^2}{(\omega - \omega_0)\omega_{\mathrm{rec}}}. \tag{5.2}$$

In our experiments, $\tau \approx 10\mu\,\mathrm{s}$.

We generally apply a KD pulse to our BEC after a couple of milliseconds of expansion time to minimize interaction effects. We record the population diffracted into the $|\pm 2\hbar k\rangle$ states and the pulse intensity profile from a diffraction beam pick-off with a photodiode (PD). Through a calibration which relates PD voltage to power, we obtain the power intensity profile. Because[1] $\Omega_R(t)^2 \propto E_0^2 \propto Intensity \propto P(t)$, the pulse intensity profile is proportional to θ by some proportionality constant a:

$$\theta = a \int P(t) dt. \tag{5.3}$$

Combining Equations 5.1.1, 5.2, and 5.3, we obtain

$$P_{max} = \frac{U_{0,max}}{\hbar 2a}. \tag{5.4}$$

The final step to obtaining the conversion is to find a. Consider the "1-1-1" point, defined as the θ where the populations in the $|\pm 2\hbar k\rangle$ are equal, which we call θ_1. To find θ_1, solve $J_0^2(\theta) = J_1^2(\theta)$ to obtain $\theta_1 = 1.43\,\mathrm{radians}$. We find experimentally which $P(t)$ produces θ_1 and obtain that

$$a = \frac{\theta_1}{\int P(t) dt}. \tag{5.5}$$

---

[1] See Chapter 2 and 7.

Combining Equation 5.4 and 5.5, we obtain

$$\frac{U_{0,max}}{\hbar} = \frac{2\theta_1}{\int P(t)dt} P_{max}. \tag{5.6}$$

The factor $\frac{1}{\omega_{\rm rec}} \frac{2\theta_1}{\int P(t)dt)}$ in Equation 5.6 is thus the conversion factor between optical power and depth.

Here are a few items to keep in mind about the calibration. Our feedback system does not work fast enough to control the intensity of the KD pulses so it is important to use the beam intensity trace to obtain the pulse area, as opposed to using an analytical form of the intensity. Using this calibration method, we had obtained values that were inconsistent with calculations and earlier calibration measurements. We realized the issue was that we were not satisfying $\tau \ll 1/\omega_{\rm rec}$ and thus we were not truly in the KD regime. Using shorter pulses pushed the calibration closer to what we expected.

There is some uncertainty in finding the "1-1-1" point. We had found it through a linear fit in diffracted population percent versus pulse area about the experimentally-found "1-1-1" point. However, the function does have some curvature which was neglected in this determination. This calibration was found to be different than one obtained in the Rabi method to be described in the subsequent section. The Rabi method produced a calibration constant which produced better agreement between theory and experiment in the experiments described in Chapter 5.

5.1.2 Rabi Method

For the Rabi method we apply a Bragg pulse and measure the diffracted fraction as a function of the pulse time. We obtain a Rabi frequency and use the calculations from the Bloch-bands calculation from Figure 2 in [25] to relate the measured Rabi

frequency to the depth. To minimize changes in depth over the course of the measurement, we use with a first-order Bragg pulse, which has the shortest Rabi period for a given power.

We used a trapezoidal intensity profile with a flat intensity section inserted in the middle. We controlled time by changing the length of the constant-intensity portion. This method meant the pulse area was simply proportional to the time, allowing us to easily increase the pulse area in equal increments. Figure 5.1 shows a sample Rabi oscillation curve whose frequency was used for a depth calibration.

5.2 Mach-Zehnder Interferometry

We performed our experiments in Mach-Zehnder (MZ) interferometer configuration which at its simplest consists of a splitting, mirror and recombination pulse. We use this simpler 2-path geometry for demonstration purposes and we plan on using the magic depth property in our contrast interferometer for future α measurements.

We will quantitatively demonstrate how a Mach-Zehnder interferometer (IFM)[32] can be used to measure the lattice-induced phase shift, schematically shown in Figure 5.2. Let the free particle eigenstate basis be labeled as $|m\rangle$, where m is some integer corresponding to a momentum state of $m\hbar k$. Let the standing waves used in the $\pi/2$ splitting pulse, π mirror pulse and $\pi/2$ recombination pulse have the phases ϕ_1, ϕ_2, and ϕ_3 respectively relative to some fixed position in the standing wave frame. This is a two-state problem involving only the $|0\rangle$ and $|2N_B\rangle$ momentum states.

In a matterwave MZ interferometer, a $\pi/2$-pulse of order N_B first puts the atomic wavefunction $|\psi\rangle$ in a superposition of the $|0\rangle$ and $|2N_B\rangle$ state at $t = 0$. The wavefunction evolves for some time T and then can be written as

$$|\Psi\rangle = \frac{1}{\sqrt{2}}\left(|0\rangle - ie^{i(\phi_1 - ET/\hbar)}\,|2N_B\rangle\right), \tag{5.7}$$

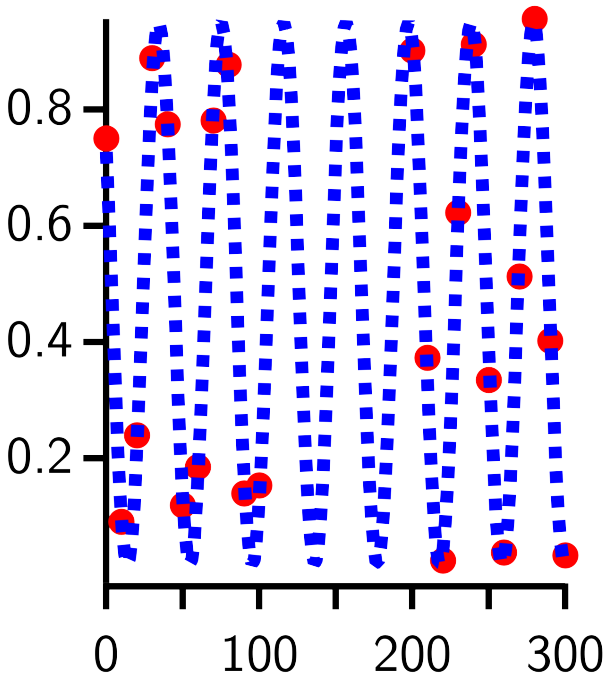

Figure 5.1 – A representative Rabi calibration curve. The fraction in the $2\hbar k$ state is shown as a function of the the constant-intensity time of the Rabi pulse.

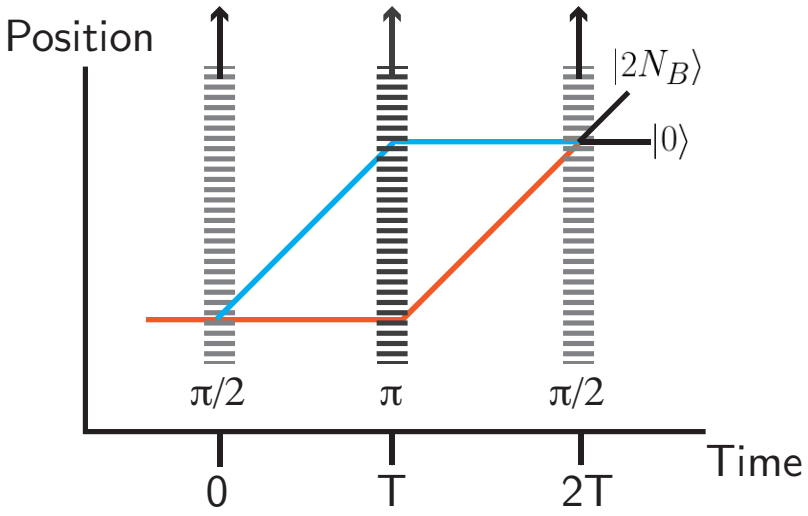

Figure 5.2 – Space-time diagram for a Mach Zehnder IFM with arm momentum separation in units of $\hbar k$ $n = 2N_B$. Each standing wave pulse is represented as a dashed line, with arrows indicating the direction of the velocity of the nodes of the standing wave. The darker π-pulse indicates it is of a higher average intensity, necessary to fully reflect each arm if the pulse times are the same.

where $E = \frac{(2N_B\hbar k)^2}{2m} = 4N_B E_r$ is the energy of a particle with momentum $p = 1N_B\hbar k$. When $t = T$, an N_B order π-pulse is applied which imparts $2N_B$ photon momenta onto either arm, accelerating them toward each other. The order of the π pulse equals the order of the $\pi/2$ pulse. The wavefunction will then have the form

$$|\Psi\rangle = \frac{1}{\sqrt{2}}\left(-ie^{i\phi_2}\,|2N_B\rangle + e^{i(\phi_1-\phi_2-ET/\hbar)}\,|0\rangle\right). \tag{5.8}$$

After evolving for an additional time T, the wavefunction is

$$|\Psi\rangle = \frac{1}{\sqrt{2}}\left(-ie^{i(\phi_2-ET/\hbar)|2N_B\rangle} + e^{i(\phi_1-\phi_2-ET/\hbar)}\,|0\rangle\right). \tag{5.9}$$

At this point the IFM arms are ideally overlapped.[2] An N_B order $\pi/2$-pulse is applied and puts the wavefunction in the state

$$|\Psi\rangle = \frac{1}{2}\left(-e^{i(\phi_1-\phi_2-ET/\hbar)} - e^{i(\phi_1-\phi_3-ET/\hbar)}\right)|0\rangle + \frac{1}{2}\left(ie^{i(\phi_1-\phi_2+\phi_3-ET/\hbar)} - ie^{i(\phi_2-ET/\hbar)}\right)|2N_B\rangle. \tag{5.10}$$

The expected population fraction in the $|0\rangle$ and $|2N_B\rangle$ state is

$$\begin{aligned} P_0 &= |\frac{1}{2}\left(e^{i(\phi_1-\phi_2-ET/\hbar)} + e^{i(\phi_2-\phi_3-ET/\hbar)}\right)|^2 = \frac{1}{2}\left(1+\cos(\phi_1+\phi_3-2\phi_2)\right) \\ P_{2N_B} &= |\frac{1}{2}\left(e^{i(\phi_1-\phi_2+\phi_3-ET/\hbar)} - e^{i(\phi_2-ET/\hbar)}\right)|^2 = \frac{1}{2}\left(1-\cos(\phi_1+\phi_3-2\phi_2)\right). \end{aligned} \tag{5.11}$$

In a typical MZ interferometer, the phase of the final $\pi/2$ pulse is varied. From Equation 5.11, it is evident that changing ϕ_i will change the populations P_0 and P_{2N_B}. The interference signal is then the final population in either state as a function of ϕ_3.

Vibrations at frequencies faster than $1/T$ will change the ϕ_i's which can limit the use of an MZ geometry for interferometry measurements. Note that this calculation neglects the diffraction phases on each arm due to the Bragg pulses.

---

[2]Repulsive interaction effects are neglected here but they can cause the inteferometer to close at times near but different than 2T. See [20].[33]

Acceleration pulses on one arm can be inserted between the $\pi/2$-pulse and π-pulse on either half of the interferometer to bring the arms further apart both in momentum and real space. A schematic for this is shown in Figure 5.3(a).

Acceleration pulses can cause a lattice-induced phase shift on the interferometer signal. Consider applying a BO pulse to the upper state which causes some phase shift ϕ_{BO} on the arm. Mathematically this looks like modifying Equation 5.7 by shifting the phase on the upper arm:

$$|\Psi(t)\rangle = \frac{1}{2}\left(|0\rangle + e^{i(\phi_1 - ET)/\hbar}\,|2N_B\rangle \rightarrow\right)|\Psi(t)\rangle = \frac{1}{2}\left(|0\rangle + e^{i(\phi_{BO}+\phi_1 - ET)/\hbar}\,|2N_B\rangle\right). \tag{5.12}$$

Carrying this modification through the rest of the calculation is mathematically equivalent to replacing ϕ_1 with $\phi_1 + \phi_{BO}$. Because the fringe phase is sensitive to ϕ_1, as seen in Equation 5.11, a lattice-induced phase shift is predicted to show up as a phase shift of the MZ fringe.

5.3 Mach-Zehnder Excited Band BO Experiments

The last section mathematically demonstrated that the MZ interferometer is predicted to be sensitive to the phase shift from BOs applied on one arm. This sensitivity allows us to study the magic depth property.

The MZ interferometer used in our lab will first be described. Let the momentum states now be denoted $|m\hbar k\rangle$. The BO pulses are applied on one arm (upper arm in Figure 5.3(a)) during the first half of the interferometer, in between the beamsplitter and mirror pulses. The $\pi/2$ splitting and recombination pulses and π mirror-pulses that compose the MZ interferometer are third-order Bragg pulses ($N_B = 3$) connecting states $|0\rangle$ and $|6\hbar k\rangle$. Between the first $\pi/2$ and π pulses, the $|6\hbar k\rangle$ (upper) arm

is accelerated to a higher momentum $|(n+6)\hbar k\rangle$ with a trapezoidal pulse applying $n/2$ BOs in the selected band. The amplitude of the wavefunction in the upper arm are then decelerated to a momentum of $6\hbar k$ with a Bragg π-pulse of order $n/2$. After the mirror pulse, the lower arm which is in a momentum state of $|6\hbar k\rangle$ is accelerated to $|(n+6)\hbar k\rangle$ using a π-pulse, it evolves for some time T, and is then decelerated to $|6\hbar k\rangle$ with a π-pulse. When the two arms are recombined and spatially overlapped, a final $\pi/2$ recombination pulse is applied. Up until this point the atoms are in a superposition state. The population in each momentum state is measured using time-of-flight absorption imaging, which projects each atom probabilistically into either the $|0\rangle$ or $|6\hbar k\rangle$ momentum state.

Each interferometer was operated at a minimal time to minimize the possible effects from vibration. To ensure the interferometer closed, the second free-evolution time was varied, increasing with increasing momentum separation. [3]

[3]The first free evolution time between the BO acceleration pulse and deceleration pulse was kept at a small $10\,\mu$s, to give enough time for digital operations.

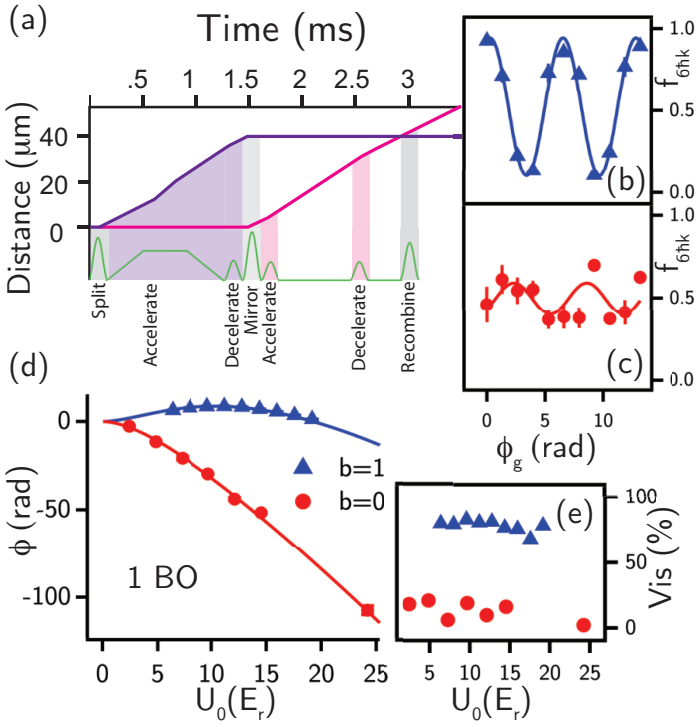
(a)
Time (ms)
.5
1
1.5
2
2.5
3
Distance (μm)
40
20
0
Split
Accelerate
Decelerate
Mirror
Accelerate
Decelerate
Recombine
(b)
(c)
f_{6hk}
1.0
0.5
0.0
0
5
10
ϕ_g (rad)
(d)
0
-50
-100
ϕ (rad)
b=1
b=0
1 BO
0
5
10
15
20
25
$U_0(E_r)$
(e)
100
50
0
Vis (%)
5
10
15
20
25
$U_0(E_r)$

We vary the phase of the recombination pulse, and build an interference signal as we record the sinisoidally-oscillating population in the $|6\hbar k\rangle$ state, as seen in Figure 5.3(b) and 5.3(c). We measure the phase of this fringe as a function of the depth of the BO pulse for ground and excited bands.

The fringe phase versus depth for one BO in the ground and excited band is shown in Figure 5.3(d). The first excited band exhibits a local maximum while the ground band a monotonically decreasing phase with lattice depth. Figure 5.3(e) shows the visibility of the sinusoidal fits. Visibility is defined as Vis $= \frac{\text{Max}-\text{Min}}{\text{Max}+\text{Min}} \times 100\%$ and Max and Min refer to the maximum and minimum of a fitted sinusoid. For a fixed number of fringes measures, the higher the visibility, the more repeatable the experiment is, corresponding to a lower phase fluctuation. More details on this relationship will be presented in Section 5.8.

5.4 Bloch-bands Magic Depth Calculations

The accumulated phase difference between the two interferometer arms due to BO then appears as a phase shift in the interferometer signal. We model this phase shift with simple calculations from our Bloch-bands model which also have a straightforward graphical interpretation. As the depth U_0 is varied, the energy of either arm of the interferometer changes, which results in a phase shift on each interferometer arm given by

$$\frac{1}{\hbar}\int_{\text{pulse}} (E(q, U_0(t)) - E_f(q(t)))dt \tag{5.13}$$

, which is the difference between the band energy $E(q(t), U_0(t))$ and free-space energy E_f(q(t)), where $U_0(t)$ and $q(t)$ depend on the BO pulse parameters. During the BO pulses, each arm, labeled 1 and 2, experiences a lattice-induced phase shift from both the inensity and frequency ramps. Since the final fringe phase depends on the

Figure 5.3 ***(previous page)*** – (a) Space-time diagram for a Mach-Zehnder interferometer with 1 BO applied to the upper path. The blue arm is the one which has been accelerated by Bloch oscillations of varying depths. Pulses affecting the upper (lower) arm only are highlighted in purple (pink). Pulse affecting both arms are highlighted in gray. Intensity profiles of the pulses are shown below in green. The representative interferometer shown has free evolution times of $10\,\mu$s and $630\,\mu$s for the first and second halves of the interferometer, respectively. The fractional population in the $|6\hbar k\rangle$ path as a function of the phase of the final recombination pulse with each point being the average of three measurements is shown in (b) and (c). For (b), one BO is performed in the first excited band ($b = 1$) near the magic depth at $U_0 = 11.2E_r$. For (c) the BO is instead performed in the ground band ($b = 0$) at a depth near the first excited band's magic depth ($9.7E_r$). The best fit sinusoids are shown. The phase of the fringe as extracted from a sinusoidal fit is plotted as a function of the depth of the BO in (d). The phase measurements are in good agreement with the phase calculated by our Bloch-bands model. The ground band is shown in red and the first excited band shown in blue. The first excited band exhibits a local maximum and thus the magic depth feature whereas the ground band does not exhibit any local extrema. In (e) the visibility of the fringe fits as a function of depth for the data collected in (c). For the first excited band, $\Delta/\Gamma = +3500$ and for the ground band $\Delta/\Gamma = +1300$. For both bands, $\dot{\delta} = 2\pi \times 83\,\mathrm{kHz/msec}$

difference between phase accrued by each arm, the interferometer phase shift due to BO can be written as:

$$\Phi_{\mathrm{BO}} = \phi_{1,I} + \phi_{1,f} - \phi_{2,I} - \phi_{2,f}, \tag{5.14}$$

where $\phi_{i,I}$ is the phase acrrued by path i during the intensity ramp and $\phi_{i,f}$ is the phase accrued by path i during the frequency ramp. Each of these phase shifts is calculated using Expression 5.13. Note that when a pulse is on and one arm is accelerated, the non-accelerated arm also experiences a smaller phase shift because it is loaded ito a higher band. It performs Landau-Zener tunneling across the narrow band gaps, which corresponds to the atom not accelerating in the lab frame. This is consistent with the fact that its momentum relative to the nodes of the lattice is increasing.

While the magic depth U_{MD} for a particular band is independent of experimental parameters, in actual experiments, the necessary intensity ramps increase the magic depth value. The phase shift due to an intensity ramp is given by Equation 5.13 where $E(q, U_0(t))$ is time-dependent because the lattice changes its depth. $E(q, U_0(t))$ is evaluated at the loading and unloading q.

Figure 5.3(d) demonstrates that in the first excited band, there is a magic depth at $U_0 \approx 10\hbar\omega_{rec}$, whereas for the ground band, only at a $U_0 = 0$ is the derivative zero.

Note that a reason we only apply a BO to one arm is because a symmetric MZ IFM is sensitive to diffraction phases. If an acceleration pulse were applied to both arms and they experienced the same phase shift, one can verify that the total phase shift on the fringe from both BO pulses would be zero. We verified that that was the case and demonstrated a fringe phase versus depth relationship is consistent with a zero-sloped line, as expected.

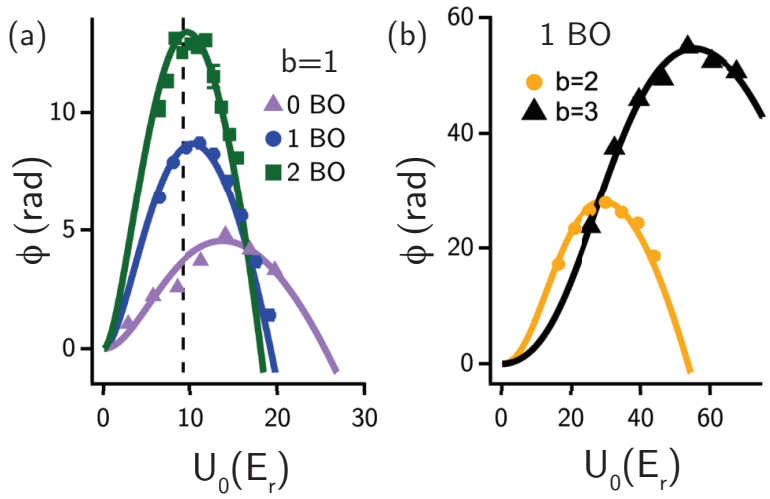

Figure 5.4 – Diffraction phase versus lattice depth U_0 for various band numbers and number of Bloch oscillations with a theory curve from a Bloch-bands calculation. (a) shows b=1 with 0, 1, 2, 3 Bloch oscillations shown in purple (triangles), blue (circles), and green (squares), respectively. The location of the magic depth as defined as $\frac{\partial\langle E\rangle}{\partial U_0} = 0$. In (b), BO with $b = 2$ (orange, circle) and $b = 3$ (black, triangles) are shown. Note that in (a) the "1 BO" data is also shown in Figure5.3(d). For all data shown $\Delta/\Gamma = +1300$, $\dot{\delta} = 2\pi \times 83\,\mathrm{kHz/msec}$, and intensity ramp times are $300\,\mu\mathrm{s}$.

5.5 More Magic Depth Experiments

We studied the phase of the interference signal for multiple Bloch oscillations in the first excited band and 1 BO in the second and third excited bands and found that we could successfully model the phase behavior of the fringes with our Bloch-bands model. Figure 5.4 shows the phase versus depth measured for these experiments.

5.6 *Efficiency of Excited Band BOs*

An important question arises: can we use excited band BOs at the magic depth to build high momentum-separation and large-area interferometers. If so, how does one choose which band is to be used. Before addressing these questions directly, this section will describe the models used to predict the efficiency of BOs in excited bands.

We model the efficiency as being reduced both by Landau-Zener losses and from spontaneous scattering. The probability of loss from Landau-Zener tunneling to a higher band is modeled with Equation 4.1. The loss at short T_{BO} is primarily dominated by Landau-Zener tunneling and for long T_{BO} by spontaneous scattering. The probability of loss due to spontaneous scattering can be calculated with two different methods. First a brief introduction to spontaneous scattering will be presented followed by a description of the two methods.

Spontaneous scattering by light is well-described by[9]. The scattering rate from one beam is given by the following equation:

$$R_{scat} = \frac{\Gamma}{2}\frac{s}{1+s+4\Delta^2/\Gamma^2}, \tag{5.15}$$

, where Γ is the transition linewidth, $s = I/I_{sat}$, I is the intensity of the light, $I_{sat} = \frac{\pi}{3}\frac{hc\Gamma}{\lambda^3}$ is the saturation intensity, and Δ is the detuning of the light from a transition. The dominant Δ contribution to the scattering rate is from the green intercombination transition, for which $I_{sat} = 1.4\,\mathrm{W/m^2}$, $\lambda = 555.8\,\mathrm{nm}$, $\Gamma = 2\pi \times 180\,\mathrm{kHz}$.

Two different ways to obtain a value for the scattering rate will be outlined. For the first method (Section 5.6.1), we calculate the intensity of the standing wave averaged over one spatial period and use that for I in Equation 5.15.

Method 1 approximates that the atoms evenly sampling all parts of the beam. However, atoms are not actually spatially homogeous; from computing the actual wavefunction of a particle in a blue-detuned sinusoidal optical potential, one finds that there is a higher probability for a particle to be found in the nodes. A particle is more likely to be found at the nodes and not the anti-nodes because the sign of the potential energy depends on the sign of the detuning (Equation 3.9). Since we use positively detuned beams ($\Delta > 0$), the potential is greater for higher intensities.

5.6.1 Method 1

For the first method, an average scattering rate assuming a homogenous density distribution is obtained and used to calculate the loss rate. For a single beam, the electric field magnitude is $E = E_0 \sin(kx - \omega t)$. The time and spatially averaged intensity is given by

$$I = \frac{c\epsilon_0}{2} E_0^2. \tag{5.16}$$

For a standing wave of light, there is scattering from two beams. For two sinusoidal beams with the same electric field E_0 propagating in the x-direction with wave number, k and $\omega = kc$, the total electric field $E_{Total} = E_0 \left(\sin(kx - \omega t) + E_0 \sin(kx + \omega t)\right) = 2E_0 \sin(kx) \cos \omega t$. Since $I = c\epsilon_0 \langle E_{Total}^2 \rangle_{space,time}$,[34]

$$I = c\epsilon_0 4E_0^2 \langle \sin^2 kx \cos^2 \omega t \rangle. \tag{5.17}$$

Averaging over $\sin^2 kx \cos^2 \omega t$, one obtains $I = c\epsilon_0 E_0^2$, the average intensity is a factor of 2 greater than the average intensity for one beam. Since scattering rate is proportional to the intensity in the limit that $\frac{4\Delta^2/\Gamma^2}{s} \gg 1$ and $\frac{\Delta}{\Gamma} \gg 1$, the average scattering rate for a standing wave is double the scattering rate of one beam in this limit. For our lowest detuning ($\Delta = 1300\Gamma$) with a typical beam power of 20 mW

and waist of 1.8 mm, $\frac{4\Delta^2/\Gamma^2}{s} = 1700 \gg 1$.

5.6.2 Method 2

The scattering rate can be more precisely obtained by finding the expectation value of the scattering rate given the wavefunction shape. This accounts for the fact that there is a higher probability for a particle to be located at a node where the intensity is lower. In Equation 5.17, if one only averages over time, one obtains

$$I = c\epsilon_0 2E_0^2 \sin^2 kx. \tag{5.18}$$

The peak intensity[4] of a single Gaussian beam is $I_{beam} = \frac{2P}{\pi w_0^2}$, where P is the power in the beam and w_0 is the waist. Setting this equal to Equation 5.16, solving for E_0, and plugging that into Equation 5.18, we obtain

$$I = \frac{8P}{\pi w_0^2} \sin^2 (kx) . \tag{5.19}$$

The results of the calculations with $w_0 = 1.8\,\text{mm}$ and $P = 22\,\text{mW}$ ($U_0 = 27E_R$) for both methods for the second excited band (b=2) is shown in Figure 5.5(a). Calculations were performed with Mathematica and Igor Wavemetrics. The second band was chosen to perform experiments with a high number of Bloch oscillations because it was found experimentally to have a higher peak efficiency out of the first, second, and third excited band.[5]

Absorption images corresponding to three different T_{BO} are shown in Figure 5.5(b). The first shows the absorption image taken for a shorter-than-optimal T_{BO}

[4] Averaged over a spatial and temporal period, peak with respect to the longitudinal and transverse distance, i.e. spatial peak.

[5] As shall be detailed in Section 5.7, the third band is predicted to have the peak efficiency. However, for the third band, the magic depth is higher, which meant that given our diffraction beam optical power budget, we needed to use a lower detuning to reach it. A lower detuning caused more spontaneous scattering, which resulted in a lower overall efficiency.

where it can be seen that Landau-Zener tunneling leads to atoms being "left behind" by the BO process. The middle image shows a T_{BO} which is nearly optimal. The final image shows atoms with a longer-than-ideal T_{BO} where spontaneous scattering limits the efficiency. In the image, there is an additional cloud with a higher momentum than the desired momentum state. We were initially puzzled by this, but it can be explained by the fact that spontaneously scattered atoms are still accelerated with the BO pulses. Specifically, the atoms which are moved to a lower band when scattering can still avoid Landau-Zener tunneling when traversing the band gaps because there are larger band gaps for lower bands. Preferentially accelerating the atoms scattered in the opposite direction of the lattice nodes' velocity is a unique feature of excited band BOs.

5.7 Higher Band Bloch Oscillations

We test the application of magic depth BOs toward large momentum separation in our Mach-Zehnder interferometer by implementing 20 BOs in the second excited band, b=2. At the magic depth in the second excited band we obtain a signal with visibility of 13%, as seen in Figure 5.5(c). [6]

How does this compare to the ground band? Our system's intensity fluctuations are at the 2% level[8], which is enough to give a 12 rad uncertainty in the phase for a ground band BO, much too high to obtain a visible signal.

The limit to our visibility was likely due to vibrations. To demonstrate, consider that a simple Monte-Carlo simulation (described in Section 5.8) of our fringe measurement returns the result that a 13% visibility is consistent with Gaussian-distributed

[6] This experiment was performed with a decelerating BO replacing the first Bragg deceleration pulse. This allowed more BO pulses to be applied for the same amount of time, before vibrations become a problem.

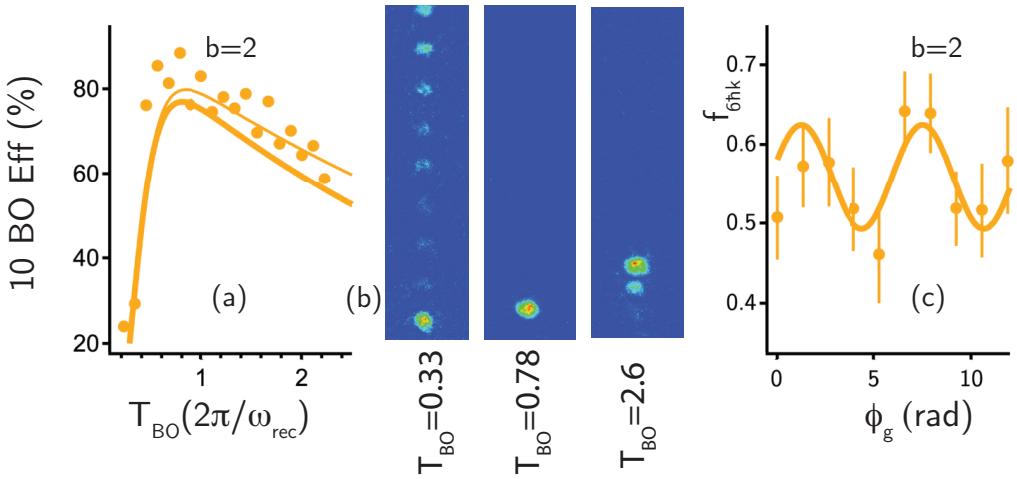

Figure 5.5 – (a) The measured efficiency versus T_{BO} for BOs performed in the second excited band (b=2) at $U_0 = 27.5\,E_r$, near the magic depth. The theoretically-expected efficiency based on Landau-Zener losses and a spontaneous scattering rate determined by method 1 (2) in section 5.6.1 (5.6.2) is shown in the thick (thin) orange line. The peak efficiency per $\hbar k$ of momentum gain was found to be 99.4%. (b) shows the absorption images corresponding to the efficiencies for three times in units of $2\pi/\omega_{\mathrm{rec}}$. (c) Shows the fringe from a Mach Zehnder interferometer with 20 BOs in the second excited band with data and a sinusoidal fit with $U_0 = 27,5\,E_r$ and $T_{BO} = 120\mu\,\mathrm{s}$. The visibility from the sinusoidal fit is 13%. $\Delta/\Gamma = +3500$ and the intensity ramp time was $300\,\mu$s for all data in the figure.

phase fluctuations with a $1/e$ radius of 2.9 rad. Our AMZ is also sensitive to the diffraction beams' mirror positions, and thus it is possible for mirror vibrations to be an additional source of phase fluctuations. Indeed, we estimate the contribution to the phase uncertainty from diffraction phases to be at $\approx$ 40 mrad, given that we estimate our intensity fluctuations to be apprxomiately 2% of the light intensity. This calculation supports the hypothesis that mirror vibrations primarily contributed to visibility reduction. Other groups have also only observed visible interferometer signals for interferometer times less than a few milliseconds.[35]

Even though excited band BOs at the magic depth allowed for achieving a 20 BOs and large momentum separation, its full utility will be realized in a vibration-insensitive interferometer. We plan to implement excited-band BOs in our next α measurement in the contrast interferometer, as described in Chapter 8. Another interferometer geometry which is insensitive to mirror vibrations is the simultaneous conjugate interferometer used by the Muller group.

We will now revisit the question of whether higher or lower bands are better for phase-stable interferometry. To explore theoretically, we used the Bloch-bands model to make predictions for excited band BOs. The value of the magic depth scales approximately quadratically with band number, as seen in Figure 5.6(a). The band gap energy $\hbar\Omega_{BG}$ corresponding to the lower value for excited bands is plotted in Figure 5.6(b). The band gap energy and spontaneous scattering (which depends on detuning) together determine the lowest Bloch period $T_{BO,Opt}$. This scales favorably with band number, meaning BOs can be performed more quickly in higher bands. The quantity $\frac{1}{2}\frac{\partial^2\langle E\rangle}{\partial U_0^2}|_{U_{MD}}U_{MD}^2$ is evaluated for each band and plotted in Figure 5.6(c), which is useful for calculating the experimentally relevant phase fluctuations from a BO performed at the magic depth. U_{MD}, $\hbar\Omega_{BG}$, and $\frac{1}{2}\frac{\partial^2\langle E\rangle}{\partial U_0^2}|_{U_{MD}}U_{MD}^2$ are all independent of the particular atom and only depend on a sinusoidal potential energy.

The next graphs in the figure depend on experimental inputs and are thus not purely related to a sinusoidal optical potential. In our case of using ^{174}Yb with 556 nm diffraction beams, $\omega_{\text{rec}} = 2\pi \times 3.7\,\text{kHz}$. Additionally we choose a reasonable representative detuning of $\Delta = 10^4\Gamma$. The optimal Bloch period $T_{BO,Opt}$ where the efficiency is maximal is calculated and plotted in Figure 5.6(d) given losses due to Landau-Zener tunneling and spontaneous scattering. This demonstrates that BOs can be performed more quickly with increasing band number. The peak efficiencies per $\hbar k$ is plotted in Figure 5.6(e). There is a local maximum at $b = 3$ which depends on the chosen parameters. Even though there is a peak efficiency, the predicted efficiency as a function of band varies weakly.

Some effects scale favorably with higher bands- namely, the band gap energy and the optimal Bloch period. On the other hand, for higher bands, the magic depth becomes higher which means more spontaneous scattering. The peak efficiency also decreases for higher depths for the representative detuning we chose, though this is detuning-dependent. The total effect on the phase fluctuations is captured in Figure 5.6(f). Assuming a 1% intensity fluctuation, the uncertainty in phase per BO is obtained by multiplying the data in Figure 5.6c by $T_{BO,Opt} \times (.01)^2$, where the $T_{BO,Opt}$ values come from Figure 5.6(d). The increasing $\Delta\phi$ indicates that lower excited bands might be a better choice for an overall more stable phase, though the $\Delta\phi$ is only weakly increasing, so it is likely that the decreasing $T_{BO,Opt}$ will play a larger role in choosing a band. The overall best choice for an interferometer would need to also take into account $T_{BO,Opt}$. More on this can be found in Chapter 8.

5.8 Visibility Simulations

Atom interferometry experiments often require the relative phases between optical lattices to not change from shot-to-shot. Mirror vibrations cause the mirrors to shift

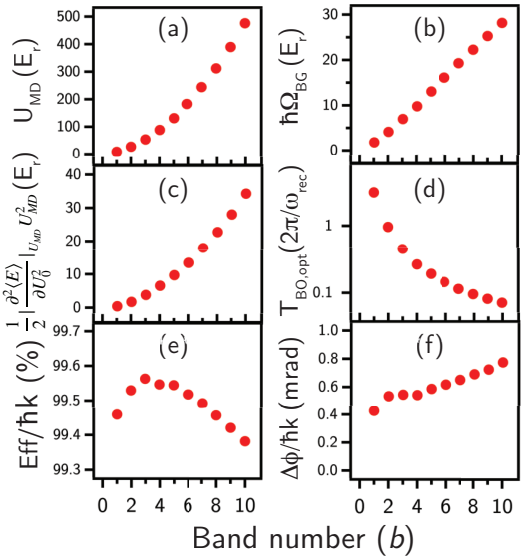

Figure 5.6 – Calculations for excited band BOs. (a) The magic depth U_{MD} as a function of band number. (b) The smallest band gap as a function of band. (c) Toward calculating the expected phase fluctuation, the quantity $\frac{1}{2}\frac{\partial^2\langle E\rangle}{\partial U_0^2}|_{U_{MD}} U_{MD}^2$ is evaluated. (d) The calculated optimal BO period, $T_{B,Opt}$. (e) The calculated peak efficiency per $\hbar k$ for $T_{BO,Opt}$ considering loses form Landau-Zener tunneling and spontaneous scattering (calculated using Method 1 in the text). (f) The calculated phase uncertainty for a single BO assuming a 1% light intensity fluctuation. For (d), (e), and (f), $\Delta/\Gamma = 10^4$ is used.

in space and constitute a serious systematic for many atom interferometry experiments and can spoil the results of the interferometer. The contrast interferometer is insensitive to vibrations, but the Mach-Zehnder interferometer used for the magic depth experiments is not. The vibrations cause the nodes to shift and constitute a phase shift on the fringe which varies shot-to-shot and reduces the visibility of the fringe.

To determine a relationship between visibility and the phase uncertainty, I created a Monte-Carlo simulation. To simulate a vibration, the function randomly picks a phase from a Gaussian distribution centered about 0 radians with a $1/\sqrt{e}$ radius of $\delta\phi$. The code then varies $\delta\phi$ and creates a variable amount of fringes and fits them with a sinusoidal fitter. The sinusoidal fitter returns a visibility. The results are shown in Figure 5.7.

In each case, the fringe is sampled at 5 different points, regardless of the total amount sampled. Each fringe had an amplitude and offset of 50. To generate the random phases, I used the "gnoise" command in IGOR. The command refers to the $1/\sqrt{e}$ radius as I verified by creating a histogram of the random phases and fitting it to a Gaussian curve with a known functional form.

For 30 experiments, there is still a sizable spread of obtained visibilities for a particular $\delta\phi$, so if visibility is used to test the $\delta\phi$, this simulation suggests more than 30 experimental points should be obtained for visibilities less than $\approx 50\%$.

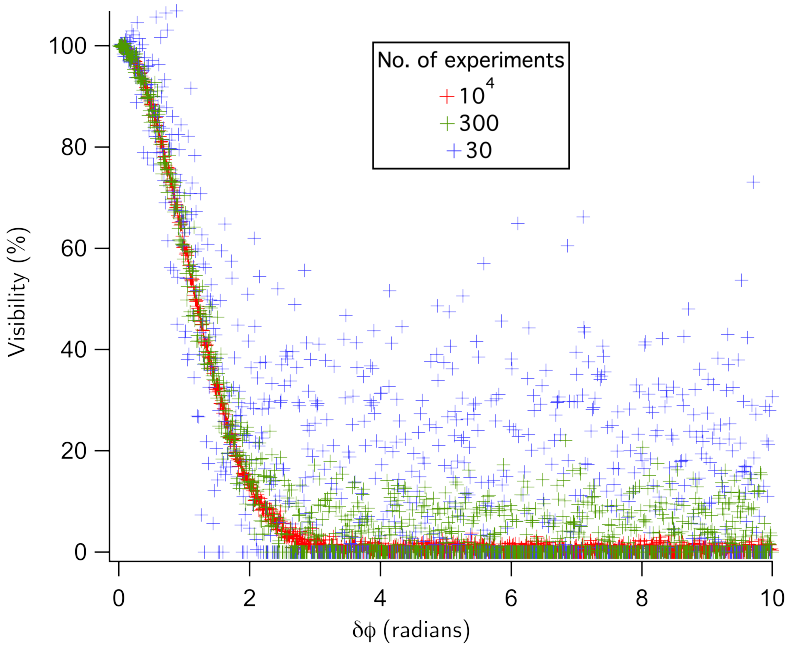

Figure 5.7 – A simulation of visibility of sinusoidal functions as a function of a random phase chosen from a Gaussian distribution with a $1/\sqrt{e}$ radius of $\delta\phi$.

Chapter 6

BEAMLINE LASER LOCK

6.1 Introduction

We can measure ω_{rec} and then calculate $\hbar/m_{Yb}$ through the relationship $\omega_{\text{rec}} = \frac{\hbar k^2}{2m_{Yb}}$. To obtain $\hbar/m_{Yb}$ from ω_{rec}, one also needs to precisely know k, the wavenumber of the light used to impart the momentum. This amounts to ensuring that the laser frequency of the diffraction beams is precisely known and carefully controlled.

The question then arises, how good does a lock need to be to not limit us in achieving our goal of a .1 ppb measurement of ω_{rec}? To investigate, we will address the question of what uncertainty in the laser frequency $\delta\nu$ is needed if the fractional uncertainty in k, $\delta k/k = .1\,\text{ppb}$. Since $\nu = \frac{ck}{2\pi}$, where c is the speed of light, then $\delta\nu = \frac{c\delta k}{2\pi}$. For 556 nm light, this amounts to $\delta\nu = 50\,\text{kHz}$.

A simple laser lock could involve directing laser light onto a vapor of atoms, scanning the laser frequency near the atomic resonance, and observing the fluorescence produced by the atoms as they decay from the excited state. The lock would electronically feed back to the laser to keep it at the frequency that produces the most fluorescence.

This method would produce a peak in fluorescence intensity versus frequency, but it would be significantly widened by Doppler broadening. Atoms moving at non-zero velocities could absorb at a shifted frequency. To estimate the width of this lock, consider that the atoms would have a speed distribution, $f(v)$, given by a Maxwell-Boltzmann distirbution for a three-dimensional gas:

$$f(v) = \frac{4\pi v^2}{(2\pi k_B T/m)^{3/2}} e^{-\frac{1}{2}mv^2/k_B T}. \tag{6.1}$$

The most probable speed is $v = \sqrt{\frac{2k_b T}{m}}$. Given that the Doppler-shifted resonance is now at ω, the Doppler shift from the resonance frequency for zero-velocity atom of ω_0 is given by the formula $\delta = \omega - \omega_0 = kc$. The most probable Doppler shift δ is thus $\delta = kv = k\sqrt{\frac{2k_b T}{m}}$. For a gas at a typical oven temperature of 500°C, this gives a shift of approximately $2\pi \times 500\,\text{MHz}$, much larger than the 50 kHz required. For a narrow lock, atoms should absorb light only within a small frequency band.

An improvement from a vapor cell would be using a beam. Traditionally, an oven nozzle is created by making an aperture in an oven with hot atoms and then making a second barrier with another aperture whose axes coincide with the first aperture which collimates the atoms into a beam. This is how our current atomic beam is created[27]. This set of apertures would filter out atoms whose velocity was not nearly parallel to the axis connecting the centers of the apertures(the atomic beam's longitudinal axis). Light could then be directed perpendicular to this longitudinal axis to preferably address atoms with minimal momentum perpendicular to the longitudinal axis ($\vec{k} \cdot \vec{v} \simeq 0$).

In this set-up, making the transverse momentum width narrow requires making the aperture smaller. However, a narrower aperture means fewer atoms. Atomic flux and momentum width are thus complementary variables; the more atomic flux demanded, the more is sacrificed in the lock linewidth. The purpose of a microcapillary nozzle, which is described below, is to create an atomic beam that has the best of both worlds: it is well collimated and can still have high atomic flux.

The key to a beamline nozzle is that in tbe opening of the oven, a nozzle is installed which consists of hundreds of stainless steel needle-like objects called microcapillaries,

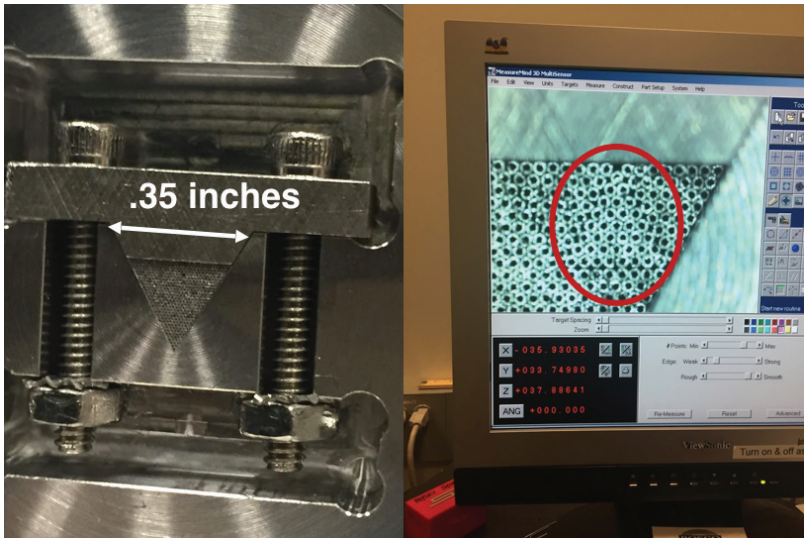

Figure 6.1 – On the left is a picture of the blank with the microcapillaries and screw plug. The right image is from the microscope in the physics machine shop of the nozzle after nearly all the microcapillaries were placed inside. One challenge to placing the microcapillaries in the nozzle is that spurious pyramids would form that made it challenging to fully fill the nozzle. For details, see Section 6.4..

as shown in Figure 6.1. An atom which is exiting the oven along the desired axis of the beam will ideally travel through a microcapillary unobstructed. The atomic flux can be kept high by stacking these microcapillaries. This strategy was pioneered by the Weld group for ^{7}Li[36]. The major way that we modified their design is that we lengthened the microcapillaries. We increased the length because we did not plan on using the atoms for any purpose other than creating a low-divergence beamline. We thus did not demand as high of number flux and we could then afford to lengthen the microcapillaries and further reduce the beam divergence.

In Section 6.2, the calculations which ultimately predict the expected Doppler

width of our signal will be detailed. In Sections 6.3 and 6.4, the design and construction of the beamline chamber and nozzle, respectively will be described. Finally, the performance of the lock and the outlook for its use in Sections 6.5 and 6.6 will be described.

6.2 Predictions

For a laser lock we can examine the fluorescence of light produced from a laser beam directed perpendicular to the atomic beam's longitudinal axis. The fluorescence curve's width is primarily still widened by Doppler broadening due to the Doppler shift in absorption frequency: $\delta = \vec{k} \cdot \vec{v}$. The Doppler width of the fluorescence curve is set by the component of the velocity that is parallel to the fluorescence beam, $v_{\parallel}$. The velocity of the exiting atoms is given by the temperature of the nozzle. The most probable speed of the atoms in an effusive beam is $u = \sqrt{\frac{3Tk_B}{m_{Yb}}}$[9]. The expected component of this velocity that is parallel to the laser light is given by the dimensions of the microcapillaries. Consider only the atoms that exit the microcapillary without any collisions with the microcapillary walls. The maximum angle with respect to the axis of the nozzle is given by the aspect ratio (AR) of the microcapillaries:

$$AR = \arctan(\frac{ID}{L}) \approx \frac{ID}{L}, \tag{6.2}$$

where ID is the inner diameter of a microcapillary and L is the length of a microcapillary (see Figure 6.2). Given the aspect ratio and average speed, the expected width of in frequency of the fluorescence signal is given by,

$$\delta = 2kuAR, \tag{6.3}$$

where the factor of two comes from the fact that atoms can exit above or below the microcapillary axis.

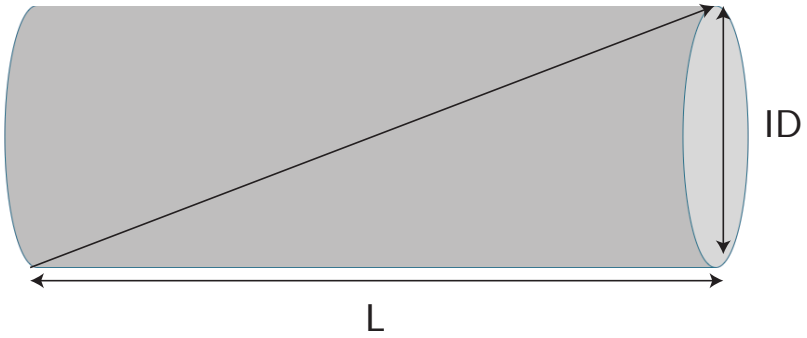

Figure 6.2 – A schematic for a microcapillary showing the inner diameter (ID) and the length (L). The diagonal represents an atom moving at a maximal divergent angle.

We used a nozzle temperature of about 500° C. The microcapillaries had an ID of 4×10^{-3} inches, and the length is 0.8 inches. This gives $\delta = 2\pi \times 6\,\mathrm{MHz}$.

6.3 Beamline Chamber

The beamline chamber is under vacuum and we used mostly MDC vacuum parts to construct it. An autocad schematic can be seen in Figure 6.3. Its constituents include:[1]

- An oven which is heated with bandheaters.
- The beamline nozzle.
- A 6-way cross and Kimball cube for optical access.
- Ion pump for creating low pressures and an ion gauge for monitoring the pressure.

[1]Details on these parts can be accessed by group members on the lab Googledrive.

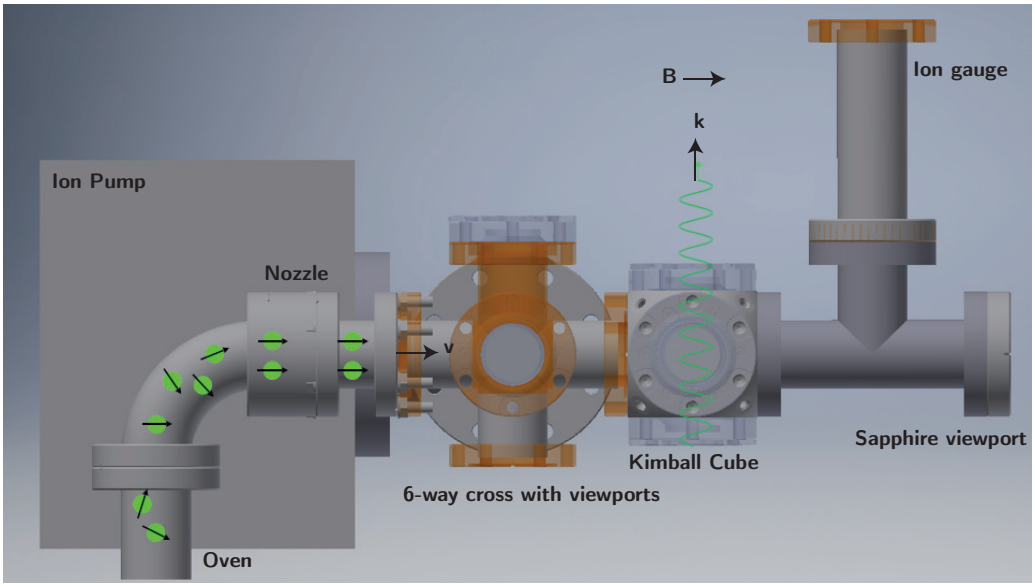

Figure 6.3 – CAD drawing from Autodesk for the beamline chamber. Atoms represented by green circles with arrows through them representing their trajectory. Ideally if an atom traverses the nozzle with microcapillaries, its velocity is nearly parallel to the beamline axis. The oven, nozzle, 6-way cross, Kimball cube, ion pump, ion gauge, and sapphire viewport are labeled.

- Viewports. All were glass (7056 glass from Duniway) except for the viewport at the end of the beamline which was made of sapphire. Sapphire was chosen because it could withstand the heating we did to it to prevent Yb from caking on its surface.

We were able to reach pressures into the 10^{-10} Torr when the oven is off.

We built magnetic coils around the beamline chamber to create a field large enough to separate the magnetic sub-levels of the $^3P_1$ excited state ($m_j = 0, \pm 1$). Each sublevel absorbs at slightly different frequencies so since there are small am-

bient magnetic field (for example, from Earth and the ion pump which contains a magnet), this will simply have a broadening effect on the excitation curve. To create a narrower spectrum, the magnetic field should be large enough such that the absorption frequency of the magnetic sub-levels are separated. We added three sets of coils: one to create a large magnetic field and two others to zero the field in the other directions. The main design considerations for building the magnetic field coils around the beamline chamber are:

- One major constraint to consider is size. The other components of the chamber and the fact that the coil rings in each dimension must properly fit with one another limits how large the rings can be.

- Given the size constraint, one could simply seek out the smallest wire. However, for a given current and number of turns, The coils should not overheat so the wires cannot be made arbitrarily small.

The magnetically insensitive excited level ($m_j = 0$) is the peak we locked to and thus for the beamline purpose, a field large enough to separate the three sub-level peaks is needed. Additional coils were added for future purposes which might demand zero-field in the other directions.

The coils have an average diameter of 3 inches. There are 200 turns on the coil that can create the largest magnetic field and 12 turns on the other dimensions.

The coils are wound in the same direction such that they produce a non-zero field in the center of the chamber. If the coils have a current I of average radius R separated by a distance d with N turns each, the magnetic field on the coil axis in the center of the chamber in between the coils is given by:

$$B = \mu_0 N I \frac{R^2}{2} \left(\frac{1}{\left(R^2 - (\frac{d}{2})^2\right)^{3/2}} + \frac{1}{\left(R^2 + (\frac{d}{2})^2\right)^{3/2}} \right). \tag{6.4}$$

For a coil with $R = 3$ inches and $d = 3$ inches, and $N = 200$, the magnetic field to current ratio is 23 Gauss/Amp.

6.4 Nozzle Construction

To design the nozzle, I used both Autodesk and then later OnShape for CAD programs. I highly recommend OnShape. The program is relatively intuitive to use, and nearly every question I had was more "Google-able" than was the case with Autodesk. I also recommend using a CAD program for any machine shop work more complicated than cutting a rectangular shape.

The nozzle is filled with grade 304 stainless steel microcapillaries bought from Microgroup. They are 0.0083" OD and 0.0043" ID with a length of 0.8" and their gauge is 33RW.

The microcapillaries were placed in a pyramid formation inside an MDC blank. A hole for the microcapillaries was made by the physics machine shop. The microcapillaries were held in place with two stainless steel screw plugs also made by the machine shop (see Figure 6.1). CAD drawings can be seen in Figure 6.3. The screwplugs were cut an additional time to fit more snugly, possibly because we ended up using less microcapillaries than we originally planned. When we suspected that atoms may be exiting the microcapillaries through unwanted channels, i.e. anywhere not through the microcapillaries, we added a copper gasket with a triangular hole machined into it for the purpose of ensuring we were blocking all the other oven exit points.

Stacking the microcapllaries was tedious. The microcapillaries bent easily and were easy to lose. Stacking imperfections in the form of spurious pyramids would crop up (see Figure 6.1). To tease out the imperfections, I "combed" the microcapillaries by running a tweezer across the microcapllaries, perpendicular to their long axis until

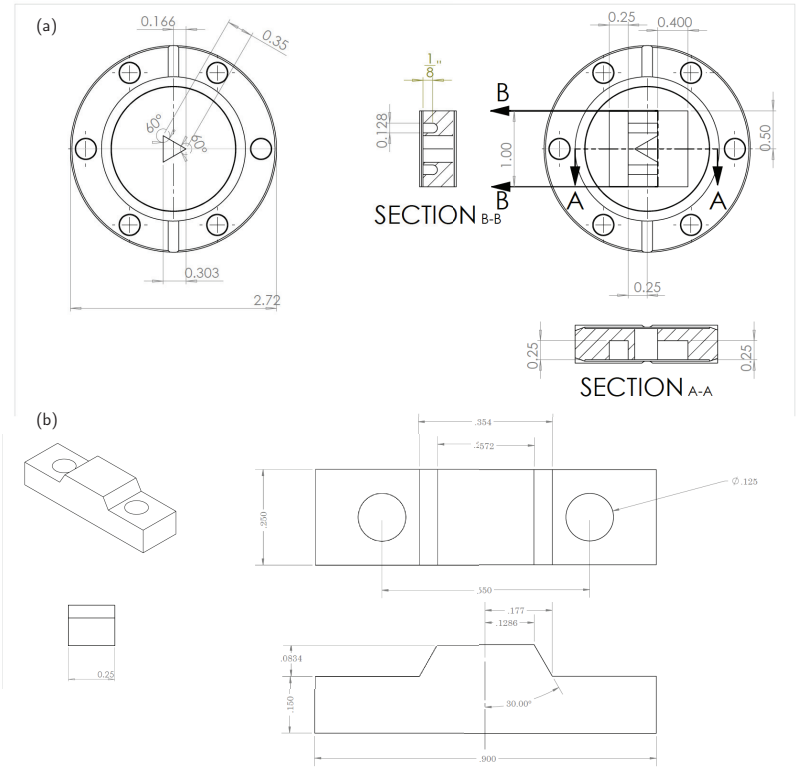

Figure 6.4 – CAD drawings for beamline blank. Both are from the Weld group. The dimensions of the screw plug were updated. All dimensions in inches.

they fell into place. I imagine if they were much longer then they could possibly be prohibitively more difficult to stack.

6.5 Evaluating the Beamline

We can lock to the peak using a lock-in technique. In our lock-in scheme, the laser scans its frequency across a fluorescence peak as the frequency of the fluoresence light is modulated at at a high frequency relative to the scan rate. The modulated lineshape is fed into a device called a lock-in amplifier, which amplifies and filters for the component of the signal which is at the frequency of modulation. It produces a signal proportional to the derivative of the signal called the error signal. For more information on this technique, I recommend Martin Zwierlein's diploma thesis[37].

We werre sucessfully able to observe three fluorescence peaks corresponding to the three Zeeman-separated m_j numbers (see Figure 6.5(a)). The central, magnetically insensitive peak is shown in Figure 6.5(b). In (c) the error signal is shown. We used powers around 10 mW.

Using the lock-in technique, we generate an error signal from the modulation of the beamline light, as seen in Figure 6.5(c). We lock the laser to the frequency where the error signal is zero, corresponding to where the fluorescence is maximal. We lock using PID control on Digilock.

We can estimate the frequency uncertainty of the beam by looking at the error signal with a frequency (f_{Laser}) dependent strength, S_{err}, and the error signal noise level during the lock, ΔS_{err}. The noise level is given by Digilock in units of S_{err} in arbitrary units. To convert this noise in error signal strength to noise in frequency, we evaluate $\frac{df_{laser}}{dS_{err}}\Delta S_{err}|_{S_{err}=0}$. To obtain $\frac{df_{laser}}{dS_{err}}|_{S_{err}=0}$, the peak-to-peak value for S_{err} of the signal can be divided by frequency separation of the minimum and maximum of S_{err}. Thus, the uncertainty of the laser frequency is frequency width divided by

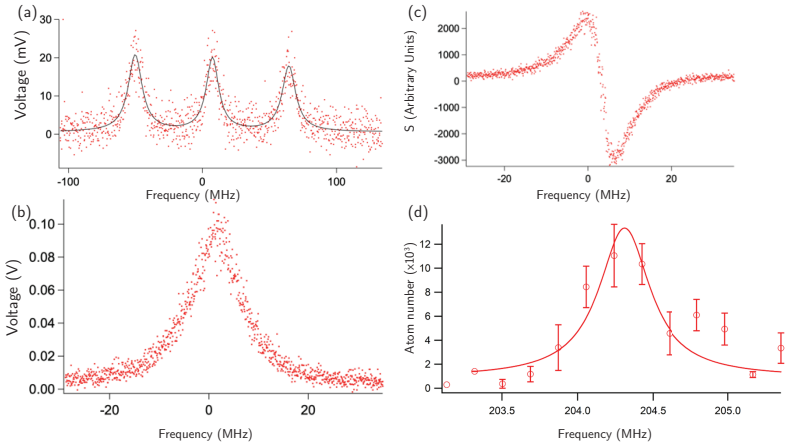

Figure 6.5 – (a) Fluorescence peaks for the three sublevels of the $^3P_1$ manifold. (b) Magnetically insensitive $m_j = 0$ state. (c) Error signal generated from modulating the fluorescence light for the $m_j = 0$ peak. (d) Atom number in absorption image as a function of MOT AOM frequency with a FWHM of 430 kHz returned from a Voigt fit.

the signal to noise ratio (SNR). An evaluation of the error signal produced a width of 7 MHz and a SNR of 10, giving an estimate of the frequency range of 700 kHz.

To further test the lock, we used green absorption imaging using MOT light. We examined the number of atoms counted as a function of the MOT AOM frequency and obtained the signal in Figure 6.5(d). The measured FWHM of the signal is 430 kHz. With a SNR of approximately 10, this puts our uncertainty in the frequency at 43 kHz. This uncertainty is low enough that we predict that the uncertainty in k would not limit a measurement of ω_{rec}. It is possible that the standard deviation for each point was increased due to technical imperfections in light intensity feedback, i.e. the light intensity may have not been the same for every shot, compromising the number measurement.

Is this lock good enough for our goal of a .1 ppb measurement of ω_{rec}? As stated

earlier in the chapter, we will investigate the question of what uncertainty in the laser frequency $\delta\nu$ is needed if the fractional uncertainty in k, $\delta k/k = .1$ ppb. Since $\nu = \frac{ck}{2\pi}$, where c is the speed of light, then $\delta\nu = \frac{c\delta k}{2\pi}$. For 556 nm light, this amounts to $\delta\nu = 54$ kHz. Comparing this calculation to our observed lock width of 43 kHz indicates that the lock would not limit an α measurement at the 0.1ppb level.

6.6 Outlook

Although we were able to obtain an error signal, it did not seem to produce a stable lock. We observed unstable BEC numbers and could not achieve CMOT temperatures of less than approximately 40 μK whereas in the past we could get it to 20 μK. The temperature of the CMOT is an indicator of the lock health because the closer one can get to resonance without going over, the colder a CMOT can be. Thus, we suspsected the lock's narrowness was a limiting factor.

One other potential fault we found with the beamline set-up was that the Thorlabs PMT (PMM02) we had in use had a maximum bandwidth of 20 kHz, which limited how fast we could modulate the intensity of light. Deep's mixture group uses modulation frequencies of 450 kHz[2] so it seemed concerning that we could not reach that level of modulation with our PMT.

Because we suspected that the lock was the issue, we went back to our beat note lock, using the mixture lab's lock as a reference (see [27] for more information on this lock).

Upon examining the beamline facts, I have come to the conclusion that it is possible that the beamline could produce a reliable lock. First, after switching back to the beatnote lock, we still experienced issues with stability in the BEC number.

---

[2]The current green modulation frequency is 111 kHz for our saturated spectroscopy lock.

Only after tuning evaporation parameters did we observe stable BEC numbers. Upon changing the lock we did not immediately observe a lower CMOT frequency. Second, the Cornish group does in fact use a 3 kHz modulation for their Yb MOT[38].

We had hoped to go the route of narrowing the fluorescence signal to observe a more stable green frequency. We reasoned that atoms with too large of a transverse velocity were being detected for our fluorescence signal. Thus, we wanted to preferentially collect fluorescence from atoms with a low transverse velocity. We reasoned that those atoms would be those closest to the center of the atomic beam, because atoms with larger transverse velocities would be displaced more in the transverse dimension. The way we planned to do this was to control which light reached our detector through a telescope consisting first of a lens, and then of a slit, as shown in Figure 6.6. With this model, we would be able to control which atoms reach the detector by changing the width of the slit.

However, this slit telescope never appeared to narrow the fluorescence signal. One reason could be related to depth of field. The atoms have a finite width along the z-axis of the telescope, so it is only possible to perfectly image one point in one plane with a particular telescope (see Figure 6.6).

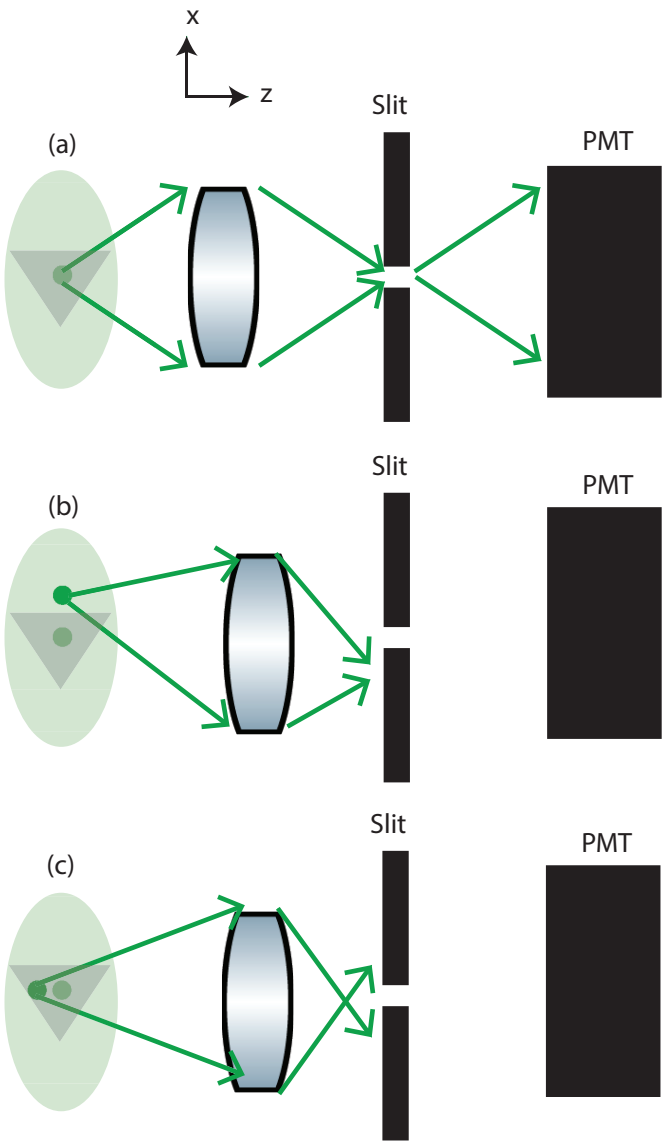

Figure 6.6 – Selectively blocking the fluorescence from atoms with a larger transverse velocity as viewed in the plane perpendicular to the atom beam propagation direction. The atom beam is represented by the light green ellipsoid and a projection of the nozzle is represented by the gray triangle. The goal is to only image atoms within the gray triangle. In (a), fluorescence from atoms in the center of the beam is focused onto the opening of a slit such that it passes to be counted by a PMT. (b) demonstrates that atoms above or below the center of the beam can be blocked with the slit. In (c), it is seen that the slit could also have the undesired effect of excluding atoms off-center along the $z - axis$.

Chapter 7

READOUT SIGNAL IN A CONTRAST INTERFEROMETER

Recall that as detailed in Section 1.6, the contrast interferometer creates an atom grating with a time-dependent contrast, oscillating between homogeneous cloud and periodic planes of atoms. Obtaining a signal involves reading the phase of traveling light that is Bragg-reflected from the matter-wave. Because the amplitude of the matterwave is time-dependent, so is the reflected signal, reflecting the most light when the matter-wave grating has the highest contrast, as seen in Figure 1.1.

In this section a model for the readout signal as a function of the various experimental parameters will be presented. For more details on the readout signal I direct the reader to either Ben[27], Alan[20], or Deep's[21] thesis.

The first contrast interferometer readout signal at UW was obtained in the physics building basement in the B063 lab space. It was a green readout signal which involved Bragg reflecting traveling diffraction beam light along k_{green} (see Fig 7.1(a)). During times of high contrast, the atoms reflected the light back along that same axis. By symmetry with respect to rotations about k_{green}, this reflection cannot be polarization-dependent.

The next iteration in the new B055 labspace involved blue readout which used our blue laser light instead of green. Since the readout light still needs to meet the Bragg condition, it must be directed at approximately a 45 ° angle with respect to the axis connecting the planes. This is precisely the reason that blue readout was used:

it was not along the diffraction axis so there was less opportunity for back-reflected light from other optics and viewports to contribute to the noise.

When this was set up, a readout signal was successfully observed. However, after some reconfiguring of the machine, the readout signal went mysteriously missing. We would attempt to reflect light at the end of an interferometer sequence but we could only observe noise. We troubleshot by checking for things including a broken photomultiplier tube (PMT), changing the readout beam size, cleaning up the mode of the readout light with a pinhole, all to no avail.

Indeed, the readout light simply needed to be the correct polarization to produce a reflecting signal along the path of the PMT, something we had not yet realized . When the blue readout light was originally set up, the polarization was luckily or unluckily at the correct polarization. Once the polarization was optimized, we nearly immediately observed strong signals, as seen in Figure 7.1. Next a model for predicting the amplitude of the readout signal will be presented where we show that the amplitude depends on the light polarization.

7.1 Classical Readout Signal Derivation

Each atom in the matter-wave formed at the closing of the interferometer can be considered as a polarizable object with polarizability α[1]. The polarizability depends on the detuning of the readout light from the ${}^1S_0 \rightarrow {}^1P_1$ transition, δ_b, the linewidth of the transition, Γ_b, the expectation value of the dipole moment, μ, and the permittivity of free space, ϵ_0.

When each atom interacts with the readout light, a dipole moment is induced. As the dipole oscillates in the presence of the incident field, it reradiates the light

[1]Not to be confused with the fine-structure constant.

in a spherical wave in the classical dipole radiation pattern. For classical dipole radiation, the radiation amplitude is maximal along the plane which perpendicular to the induced dipole moment. The induced dipole moment is along the same axis as the incident electric field, which by definition is the direction of polarization of the incident electric field. The radiation monotonically decreases to zero along the polarization axis.

Bragg reflection relies on coherence between the oscillators. For solid state crystals, that is the electrons in a lattice of ions. In our experiment, there are atoms making up the matterwave which are the oscillators. The radiation from each atom in the matter-wave must add constructively in order to observe a reflection signal from the atoms. If the polarization is set to be along the axis along a plane then the radiation will add coherently and the intensity of the reflected light will be maximal along a path shown in Figure 7.1(b), as desired.

Consider a polarizable object in the presence of a sinusoidal electric field with wave vector k and wavelength λ. When observing at large distances r from the dipole of size d ($r \gg \lambda \gg d$), the electric field, $\vec{E}$, and magnetic field, $\vec{H}$ take on form

$$\vec{H} = \frac{ck^2}{4\pi} (\hat{r} \times \vec{p}) \frac{e^{ikr}}{r} \tag{7.1}$$

$$\vec{E} = Z_0 \vec{H} \times \hat{r} \tag{7.2}$$

where c is the speed of light, $\vec{p}$ is the dipole moment, $\vec{r}$ is a unit vector in the direction of observation, and $Z_0 = \sqrt{\frac{\mu_0}{\epsilon_0}}$. Combining these two equations to solve for the electric field yields

$$\vec{E} = \frac{ck^2}{4\pi} \frac{e^{ikr}}{r} Z_0 (\vec{p} - (\vec{p} \cdot \hat{r}) \hat{r}) \tag{7.3}$$

For the case of an object with a polarizability α, $\vec{p} = \alpha \vec{E}_{inc}$, where $\vec{E}_{inc}$ is the incident electric field which causes the object to get polarized. This formula predicts that

$\vec{E}$ will be zero along the axis parallel to $\vec{E}$ and maximal in the plane where $\vec{p}$ is perpendicular to $\hat{r}$.

We now turn towards applying this model to predicting the maximal radiated electric field from ^{174}Yb in the electronic ground state. The atom can be modeled as a polarizable object[39] with

$$\alpha = -\frac{\mu^2}{\epsilon_0 \hbar} \frac{1}{\delta_b^2 + \Gamma_b^2/4} \left(\delta_b - i\Gamma_b/2\right). \tag{7.4}$$

In this equation, μ is the electric dipole matrix element connecting the ground and $^1P_1$ excited state and $\delta_b = \omega_{light} - \omega_0$ where $\hbar\omega_0$ is the energy difference between the ground and excited state and ω_{light} is the angular frequency of the incident light.

Consider the case where light is incident upon the atoms at the proper angle such that it satisfies the Bragg condition. The Bragg condition requires that $2d\cos\theta = m\lambda_{light}$, where d is the spacing between lattice sites, θ is the angle of incidence (see Figure 7.1), and λ is the wavelenght of the incident light and m is an integer. For the case of our matterwave, when contrast is maximal, there is a grating with a spatial periodicity of $d = \lambda_g/2$. Given that we are using blue readout light ($\lambda_{light} = 399\,\text{nm}$) and $\lambda_g = 556\,\text{nm}$, to satisfy the Bragg condition, the incident angle should be $44\,^\circ$. Define the $\hat{n}$ axis where we expect maximal reflection at $44\,^\circ$ clockwise from the y-axis.

As reasoned earlier in the section, to cause the atoms to radiate such that their wavefronts add constructively, the polarization of the incident light must be parallel to the planes of atoms in the matterwave. In the coordinate system shown in Figure 7.1, this is in the z-direction. Since $\vec{p} = \alpha\vec{E}$, $\vec{p}$ then points in the $\hat{z}$ direction.

Taking into account that $\vec{p} = \alpha E_{inc}\hat{z}$, letting $\vec{n}$ pointing $44\,^\circ$ clockwise from the y-axis and in particular perpendicular to $\vec{p}$, and the form of α found in Equation 7.4,

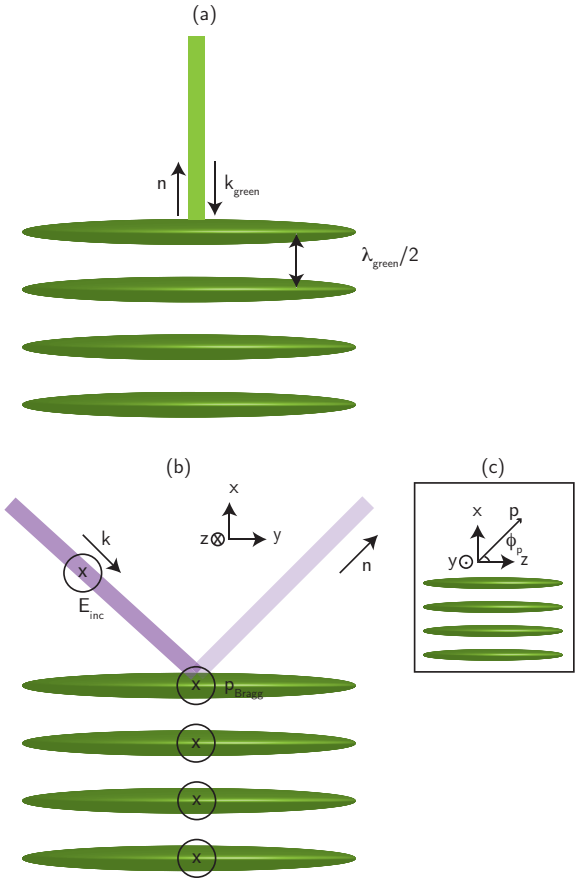

Figure 7.1 – The top figure (a) demonstrates green readout for our contrast interferometer for a time of maximum grating contrast. The green ellipsoids represents the planes of atoms which Bragg reflect the traveling waves of light. The bottom figure (b) demonstrates blue readout schematically for a polarization p_{Bragg} where reflection is maximal. Figure (c) shows a view of (b) rotated around the $x-$axis to demonstrate ϕ_p. Figures not to scale.

Equation 7.3 simplifies to

$$\vec{E} = -\frac{ck^2}{4\pi}\frac{e^{ikr}}{r}Z_0\left(E_{inc}\frac{\mu^2}{\epsilon_0\hbar}\frac{1}{\delta_b^2+\Gamma_b^2/4}\left(\delta_b - i\Gamma_b/2\right)\right)\hat{z} \tag{7.5}$$

This is the electric field due to one oscillator radiating along $\hat{n}$. Of course it is key to the reflection that many atoms are oscillating such that their radiation constructively interferes. In the case of perfect interference, the electric field is multiplied by a factor of N, the number of atoms contributing to the signal. Finally, to compute the expected intensity we use $I = \langle \vec{E} \times \vec{H} \rangle$ and Equation 7.2 to obtain

$$I = N^2\left(\frac{ck^2}{4\pi^2 r}\right)^2 Z_0\left(\frac{\mu^2}{\epsilon_0\hbar}\frac{1}{\delta_b^2+\Gamma_b^2/4}\right)^2\left(\delta_b^2 - \Gamma_b^2/4\right)E_{inc}^2. \tag{7.6}$$

To compute the intensity as a function of the incident light's polarization angle, consider the case of light polarized in the x-y plane and perpendicular to the incident light's k-vector. The radiation from each atom would no longer add constructively and one would expect no Bragg scattering from the readout light. The general incident light polarization can be decomposed into this polarization which produces no radiation and the polarization in the z-dimension. Thus, the electric field and radiated intensity can be modified with a multiplicative factor of $\cos\phi_p$ and $\cos^2 phi_p$, respectively, where ϕ_p is the polarization angle with respect to rotations about $\vec{k}$ where $\phi_p = 0$ means the polarization is along the positive z-dimension.

The signal amplitude experimentally demonstrates this dependence on readout light polarization angle. As a function of the waveplate angle, the signal strength oscillates sinusoidally, as seen in Figure 7.2.

7.2 Readout Detuning

A question arises: what is the optimal detuning for the readout beam (δ_b)? A detuning too far from resonance will not sufficiently excite the dipole radiation from

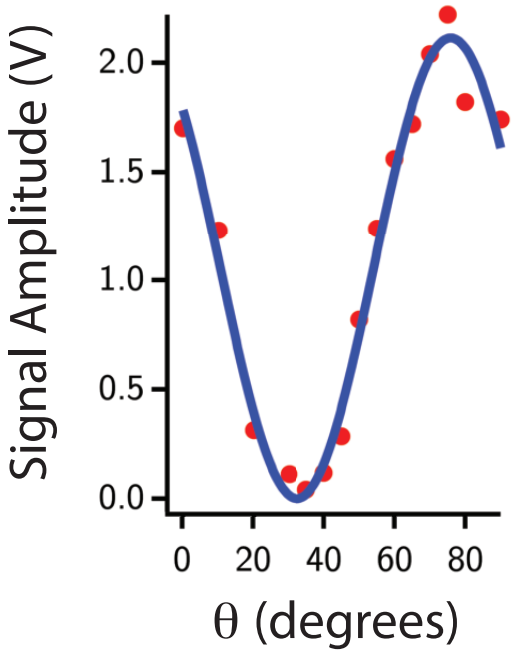

Figure 7.2 – The maximum signal amplitude as a function of half-wave plate angle. Note that when a half-wave plate is rotated by some angle θ, the polarization rotates by 2θ, so the periodicity of the polarization has the expected 180° period. A fit of a $\cos^2\theta$ function is shown which returned the expected period of 90°.

the atoms. A detuning too close to resonance can cause spontaneous scattering and also affect the index of refraction. This section will sketch out some of the ideas which can be used to model the reflection amplitude as a function of the detuning.

In the limit of $\delta_b \gg \Gamma_b$, Equation 7.6 tells us that the readout intensity, I, is proportional to $1/\delta$.

The spontaneous scattering rate is given by Equation 5.15. In the limit of $1 + s \ll 1$, $R_{scat} \propto \frac{1}{\delta}$. Thus, the detuning should be chosen under the constraint that $R_{scat} t_{coherence}$ is kept small, where $t_{coherence}$ characterizes the time width of the reflected signal.

A final effect which we consider is the index of refraction shift across the cloud (in the $x-$dimension as represented in Figure 7.1). If the shift is too large, the reflections from each Bragg plane would no longer be coherent due to the wavelength of light traveling in the cloud with a shifted wavelength: $\lambda \to \frac{\lambda}{n_r}$, where n_r is the real part of the index of refraction. Thus, the constrant that the change in phase shift across the cloud of size Δx for $n_r = 1 \to n \neq 1$ should be small:

$$\delta\phi_x \equiv k_b \Delta x - n_r k_b \Delta x \ll 2\pi. \tag{7.7}$$

To write this constraint in terms of detuning, one can obtain the index of refraction from Equation 7.4, which gives the polarizability α in terms of δ_b. The index of refraction n is given by

$$n = \sqrt{\frac{\epsilon}{\epsilon_0}} = \sqrt{1 + \rho\alpha}, \tag{7.8}$$

where ρ is the atomic density. Approximating that $\alpha \ll 1$, $n_r - 1 \propto \frac{1}{\delta_b/\Gamma_b}$, Equation 7.7 becomes

$$\frac{k_b \Delta x}{\delta_b/\Gamma_b} \ll 2\pi. \tag{7.9}$$

Chapter 8

OUTLOOK

8.1 Sensitivity

In our next iteration of the contrast interferometer we plan to use a vertical diffraction beam geometry, as detailed in [27]. We also plan to incorporate Bloch oscillations at the magic depth. This chapter will describe how we can use these changes to increase our measurement precision. In all derivations, we assume the use of simultaneous Bloch oscillations, as opposed to sequentially addressing each arm.

As explained in Chapter 1, in our contrast interferometer, we measure the phase Φ of the contrast signal at $t = 2T$ which is given by

$$\Phi(2T) = \frac{1}{2} n^2 \omega_{\text{rec}} \Delta T + \phi_{\text{offset}}, \tag{8.1}$$

where n is the maximum momentum separation between the outer arms of the interferometer in units of $\hbar k$, ΔT is the range free evolution times during one half (in time) of the interferometer, and ϕ_{offset} is the phase offset, independent of T. From our measurement of $\Phi(2T)$, we measure ω_{rec}. The part of the overall uncertainty in $\frac{\delta\omega_{\text{rec}}}{\omega_{\text{rec}}}$ which comes from the uncertainty in the phase is given by

$$\frac{\delta\Phi\left(N_{BO}\right)}{\Phi(2T)} = \frac{\delta\Phi(N_{BO})}{\frac{1}{2} n^2 \omega_{\text{rec}} \Delta T \sqrt{M}}, \tag{8.2}$$

where $\delta\Phi(N_{BO})$ is a statistical uncertainty in the phase of the contrast readout signal, M is the number of experimental shots, and N_{BO} is the total number of BO

applied to both arms. There is an implicit dependence of n on N_{BO}.

To be clear on the definition of N_{BO}, an example is given. To accelerate the outer arms of the interferometer from $|\pm 2\hbar k\rangle$ to $|\pm 4\hbar k\rangle$ ($\Delta n = 4$), 8 pulses are applied: two acceleration and deceleration for either arm for each half in time of the interferometer. Thus $N_{BO} = 8$ in this case. Generalizing from this example,

$$N_{BO} = 2\Delta n. \tag{8.3}$$

Neglecting the momentum separation due to the KD pulse and any other sources of momentum separation, we can write

$$N_{BO} = 2n. \tag{8.4}$$

We consider two ways that increasing the number of BOs can increase the uncertainty in $\delta\phi/\Phi(2T)$: first, by changing the total atom number, and second, by changing the phase fluctuation range from lattice-induced phase shifts.

8.2 Phase uncertainty

8.2.1 Lattice-Induced Phase Shift Phase Uncertainty

The phase uncertainty due to a second-order contribution from lattice-induced phase shifts $\Delta\phi_{LI}$ is estimated by calculating

$$\Delta\phi_{LI} = N_{BO}\frac{1}{2}\left|\frac{\partial^2\langle E\rangle}{\partial U_0^2}\right|_{U_{MD}} \Delta U_{MD}^2 \mathrm{T}_{\mathrm{BO,opt}}. \tag{8.5}$$

To evaluate $\Delta\phi_{LI}$, I used the values obtained from Fig. 5.6(c) and (d) for $\frac{1}{2}\left|\frac{\partial^2\langle E\rangle}{\partial U_0^2}\right|_{U_{MD}} U_{MD}^2$ and $\mathrm{T}_{\mathrm{BO,opt}}$. We also use $\Delta U_{MD}^2 = (U_{MD}\cdot\beta)^2$ where $\beta\times 100$ is the percent fluctuation

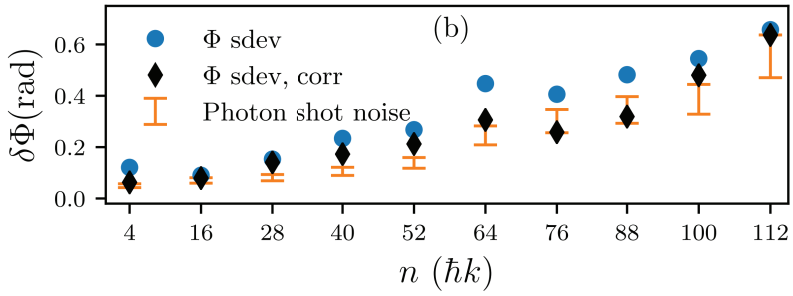

Figure 8.1 – The uncertainty in the phase of our readout signal as a function of the momentum separation in the 2018 iteration of the contrast interferometer. Plot taken from Figure 2 of [8].

range of U_0. Numerically for the third band, this equation is

$$\Delta\phi_{LI} = N_{BO}(3.8)(.01^2)(0.45)2\pi, \tag{8.6}$$

where we estimate that the depth fluctuation range is 1% of the depth, using $f = 0.01$.

8.2.2 Atom-loss Related Uncertainty

The number loss from finite BO efficiencies can also increase the uncertainty of the measurement. The relationship between N_{BO} and the phase uncertainty due the final atom number dependence on the pulse efficiency $\Delta\phi_{eff}$ can be calculated by examining Figure 8.1.

In this figure $\Delta\phi_{eff}$ is shown to depend on the maximum momentum separation of the arms in units of $\hbar k$, n, because as n increases, the atom number decreases. Thus, the horizontal axis could be converted to atom number. Atom number is also related to N_{BO} due to the efficiency of Bloch oscillations, as seen in Fig. 5.6(e). Through this relationship, there exists a linear conversion between n for the experiments in

[8] and N_{BO} which produce the same overall efficiency, eff_0. To prove this linear relationship, let the efficiency for simultaneous BOs per $\hbar k$ be eff_{BO} and the per $\hbar k$ efficiency for a third-order Bragg pulses used in [8] be eff_{Bragg}.

$$\text{eff}_0 = \text{eff}_{BO}^{2N_{BO}} = \text{eff}_{Bragg}^{6N_{Bragg}}. \tag{8.7}$$

where N_{Bragg} is the number of Bragg pulses and the exponent of eff_{BO} is $2N_{BO}$ because each BO imparts a momentum of $2\hbar k$ and the exponent of eff_{Bragg} is $6N_{Bragg}$ because each Bragg pulse produces a momentum change of $6\hbar k$.

Taking a logarithm of both sides and solving for N_{BO} shows that N_{BO} and N_{Bragg} have a linear relationship:

$$N_{BO} = 3N_{Bragg}\frac{\log(\text{eff}_{Bragg})}{\log(\text{eff}_{BO})}. \tag{8.8}$$

For our estimations, we approximate the relationship between N_{Bragg} and $\Delta\phi_{eff}$ as linear (Figure 8.1), we then conclude that the relationship between $\Delta\phi_{eff}$ and N_{BO} is also linear.

To determine the relationship between $\Delta\phi_{eff}$ and N_{BO}, we start by solving for the overall efficiency for two different N_{Bragg} using $\text{eff}_{Bragg} = 0.984$[8] and $\text{eff}_{BO} = 0.996$ (Figure 5.6). We will then solve for the number of Bloch oscillations which produces either overall efficiency to obtain the desired relationship between $\Delta\phi_{eff}$ and N_{BO}.

From the graph on Figure 8.1, $n_{2018} = 88$ and $n_{2018} = 52$ were evaluated.[1] For either n_{2018}, the number of third-order pulses (N_{Bragg}) is to be determined. In our contrast interferometer, we increased n_{2018} by $4\hbar k$ from the Kapitza-Dirac splitting pulse. Second, each set of two Bragg pulses applied to the outer arms increased n_{2018} by $12\hbar k$. Third, each set of pulses needs to be applied 4 times (acceleration and deceleration in either half of the interferometer). There is also a first-order mirror

[1] I am using n_{2018} to specify that the momentum separation for the interferometer in [8].

pulse that we approximate has the same per-$\hbar k$ efficiency as the third-order pulses. Thus, for $n_{2018} = 88$, $(88-4)/12 \cdot 4 \cdot 2 + 1 = 57$ ($N_{Bragg} = 57$)pulses were used and for $n_{2018} = 52$, $(52-4)/12 \cdot 4 \cdot 2 + 1 = 33$ ($N_{Bragg} = 33$) pulses were used. We neglect the atom loss due to a finite efficiency of the KD pulse. Using Equation 8.8, We obtain that for $N_{Bragg} = 57$, $N_{BO} = 670$ and for $N_{Bragg} = 33$, $N_{BO} = 388$. From Figure 8.1, We estimate the difference in $\Delta\phi_{eff}$ between $n_{2018} = 88$ and $n_{2018} = 52$ to be $\simeq 0.25$ radians. Thus, for an increase in the number of Bloch oscillations by $\Delta N_{BO} = 670 - 388 = 282$, the phase uncertainty increases by $\simeq 0.25$ radians. Finally we can use Equation 8.1 to obtain that for the third band,

$$\Delta\phi_{eff} = \frac{.25\text{rad}}{282} N_{BO} = \frac{.25\text{rad}}{282} 2n. \tag{8.9}$$

Similar calculations can be performed for other bands. To summarize this subsection, the goal was to find the uncertainty in the phase due to the finite-efficiency of the pulses because their finite efficiency means that less atoms are participating in the signal with increasing momentum separation. The relationship between $\Delta\phi_{eff}$ and momentum separation n was found for the interferometer reported on in [8] and is seen in Figure 8.1. Because we predict we can use higher-efficiency BO pulses, the x-axis of Figure 8.1 is to be scaled to find the predicted relationship between $\Delta\phi_{eff}$ and n for the future interferometer. For a BO with per $\hbar$k efficiency of 0.996, the relationship between $\Delta\phi_{eff}$ and n is obtained.

8.3 Total Uncertainty

To obtain the total phase as a function of the number of BOs, we evaluate

$$\Phi(2T) = \frac{1}{2} n^2 \omega_{\text{rec}} \Delta T. \tag{8.10}$$

Let the maximimum total interferometer time be T_{max} and assume BOs are performed at the optimal period, $T_{BO,Opt}$ (see Figure 5.6.) Given that half of the total

number of BOs are performed in either half of the interferometer, the maximum time for ΔT is thus $T_{max}/2 - (N_{BO}/2)T_{BO,Opt}$ and thus the total phase can be written as

$$\Phi(2T) = \frac{1}{2} n^2 \omega_{\text{rec}} \left(\frac{T_{max}}{2} - \frac{N_{BO}}{2} T_{BO,Opt} \right). \tag{8.11}$$

Combining Equation 8.11 with the quadrature sum of the uncertainty from Equations 8.9, and 8.6 and using Equation 8.1, we obtain the following form of the uncertainty:

$$\frac{\delta\Phi}{\Phi} = \frac{\sqrt{\Delta\phi_{eff}^2 + \Delta\phi_{LI}^2}}{\frac{1}{2} n^2 \omega_{\text{rec}} \frac{1}{2} \left(T_{max} - 2nT_{BO,Opt}\right) \sqrt{M}}, \tag{8.12}$$

where $\Delta\phi_{eff}$ is given by Equation 8.9 and $\Delta\phi_{LI}$ is given by Equation 8.6.

Using a 3 second cycle time and letting the data set be taken over 10 hours, we obtain $M = 12000$. For the new vertical geometry, from estimates made in [27], the total interferometer time is about 200 ms or 100 ms for each half of the interferometer. As a function of n, in band 3, $\frac{\delta\Phi}{\Phi}$ has the behavior shown in Figure 8.2. The minimum uncertainty is about 0.005 ppb for $n = 412$.

Similar calculations can be performed for the other bands. The results are printed in Figure 8.2.

The minimum uncertainty decreases with band number because for increasing band, the BOs can be performed more efficiently.

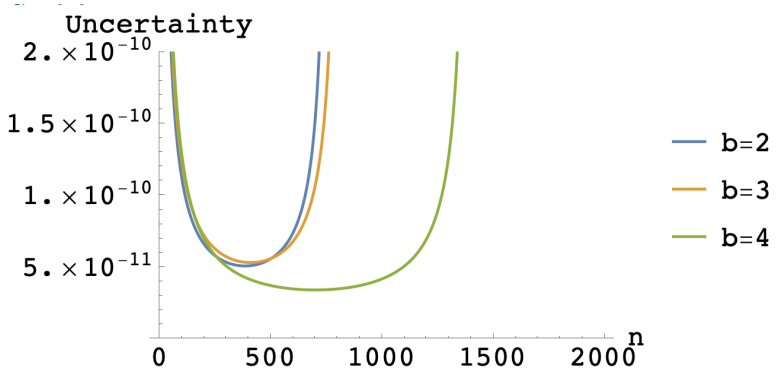

Figure 8.2 – The phase uncertainty $\frac{\delta\Phi}{\Phi}$, as a function of the maximum momentum separation (n) for bands 2, 3, and 4.

BIBLIOGRAPHY

[1] Parker, R. H., Yu, C., Estey, B., Zhong, W. and Muller, H. "Measurement of the fine-structure constant as a test of the Standard Model." *Science*, 360, 191 (2018).

[2] Hanneke, D., Fogwell, S. and Gabrielse, G. "New Measurement of the Electron Magnetic Moment and the Fine Structure Constant." *Phys. Rev. Lett.*, 100, 120801 (2008).

[3] Odom, B., Hanneke, D., D'Urso, B. and Gabrielse, G. "New Measurement of the Electron Magnetic Moment Using a One-Electron Quantum Cyclotron." *Phys. Rev. Lett.*, 97, 030801 (2006).

[4] Sorrentino, F., Bertoldi, A., Bodart, Q., Cacciapuoti, L., Angelis, M. D., Lien, Y.-H., Prevedelli, M., Rosi, G. and Tino, G. M. "Simultaneous measurement of gravity acceleration and gravity gradient with an atom interferometer." *Applied Physics Letters*, 101, 11, 114106 (2012).

[5] Holmgren, W., Revelle, M., Lonij, V. and Cronin, A. "Absolute and ratio measurements of the polarizability of Na, K, and Rb with an atom interferometer." *Physical Review A*, 81, 5 (2010).

[6] Durfee, D., Shaham, Y. and Kasevich, M. "." *Phys. Rev. Lett.*, 97, 240801 (2006).

[7] Jamison, A. O., Plotkin-Swing, B. and Gupta, S. "Advances in Precision Contrast Interferometry with Yb Bose-Einstein condensates." *Phys. Rev. A*, 90, 063606 (2014).

[8] Plotkin-Swing, B., Gochnauer, D., McAlpine, K., Cooper, E., Jamison, A. and Gupta, S. "Three-Path Atom Interferometry with Large Momentum Separation." *Phys. Rev. Lett.*, 121, 133201 (2018).

[9] Foot, C. J. Atomic physics. Oxford master series in atomic, optical and laser physics. Oxford University Press, Oxford (2007).

[10] Abbott, B. P. and et. al. "Observation of Gravitational Waves from a Binary Black Hole Merger." *Phys. Rev. Lett.*, 116, 061102 (2016).

[11] Shevchenko, S., Ashhab, S. and Nori, F. "Landau–Zener–Stückelberg interferometry." *Physics Reports* (2010).

[12] Duca, L., Li, T., Reitter, M., Bloch, I., Schleier-Smith, M. and Schneider, U. "An Aharonov-Bohm interferometer for determining Bloch band topology." *Science*, 347, 6219, 288 (2015).

[13] Bloch, F. "Über die Quantenmechanik der Elektronen in Kristallgitter." *Z Phys*, 52, 555 (1928).

[14] Waschke, C., Roskos, H., Schwedler, R., Leo, K., Kurz, H. and Kohler, K. "Coherent Submillimeter-Wave Emission from Bloch Oscillations in a Semiconductor Superlattice." *Phys. Rev. Lett.*, 70, 3319 (1993).

[15] Ben Dahan, M., , E., Reichel, J., Castin, Y. and Salomon, C. "Bloch Oscillations of Atoms in an Optical Potential." *Phys. Rev. Lett.*, 76, 4508 (1996).

[16] Wilkinson, S., Bharucha, C., Madison, K., Niu, Q. and Raizen, M. G. "Observation of Atomic Wannier-Stark Ladders in an Accelerating Optical Potential." *Phys. Rev. Lett.*, 76, 4512 (1996).

[17] Peik, E., Ben Dahan, M., Bouchoule, I., Castin, Y. and Salomon, C. "Bloch oscillations of atoms, adiabatic rapid passage, and monokinetic atomic beams." *Phys. Rev. A*, 55, 2989 (1997).

[18] Battesti, R., Clade, P., Guellati-Khelifa, S., Schwob, C., Gremaud, B., Nez, F., Julien, L. and Biraben, F. "Bloch Oscillations of Ultracold Atoms: A Tool for a Metrological Determination of h/m_{Rb}." *Phys. Rev. Lett.*, 92, 253001 (2004).

[19] Anderson, M. H., Ensher, J. R., Matthews, M. R., Wieman, C. E. and Cornell, E. A. "Observation of Bose-Einstein Condensation in a Dilute Atomic Vapor." *Science*, 269, 5221, 198 (1995).

[20] Jamison, A. O. "Precision Interferometry with Bose-Einstein condensates." Ph.D. thesis, University of Washington (2014).

[21] Gupta, S. "Experiments with Degenerate Bose and Fermi Gases." Ph.D. thesis, Massachusetts Institute of Technology.

[22] Roy, R., Green, A., Bowler, R. and Gupta, S. "Rapid cooling to quantum degeneracy in dynamically shaped atom traps." *Phys. Rev. A.*, 93, 043403 (2016).

[23] Jamison, A. O., Kutz, J. N. and Gupta, S. "Atomic Interactions in Precision Interferometry Using Bose-Einstein Condensates." *Phys. Rev. A.*, 84, 043643 (2011).

[24] Gupta, S., Leanhardt, A. E., Cronin, A. D. and Pritchard, D. E. "Coherent Manipulation of Atoms with Standing Light Waves." *Cr. Acad. Sci. IV-Phys*, 2, 479 (2001).

[25] Gochnauer, D., McAlpine, K. E., Plotkin-Swing, B., Jamison, A. O. and Gupta, S. "Bloch-band picture for light-pulse atom diffraction and interferometry." *Phys. Rev. A*, 100, 043611 (2019).

[26] National Academy of Sciences. Biographical Memoirs: V.64. The National Academies Press, Washington, DC (1994).

[27] Plotkin-Swing, B. T. "Large Momentum Separation Matter Wave Interferometry." Ph.D. thesis, University of Washington.

[28] Morsch, O. and Oberthaler, M. "Dynamics of Bose-Einstein condensates in optical lattices." *Rev. Mod. Phys.*, 78, 179 (2006).

[29] Zener, C. "Non-adiabatic crossing of energy levels." *Proc. R. Soc. London A*, 137 (1932).

[30] Hecker Denschlag, J., Simsarian, J. E., Haffner, H., McKenzie, C., Browaeys, A., Cho, D., Helmerson, K., Rolston, S. and Phillips, W. D. "A Bose-Einstein condensate in an optical lattice." *J. Phys. B.*, 35, 3095 (2002).

[31] Ovchinnikov, Y. B., Müller, J. H., Doery, M. R., Vredenbregt, E. J. D., Helmerson, K., Rolston, S. L. and Phillips, W. D. "Diffraction of a Released Bose-Einstein Condensate by a Pulsed Standing Light Wave." *Phys. Rev. Lett.*, 83, 284 (1999).

[32] Young, B., Kasevich, M. A. and Chu, S. "Precision Atom Interferometry with Light Pulses." *Atom Interferometry* (edited by P.Berman, Academic Press, New York, 1997.).

[33] Simsarian, J. E., Denschlag, J., Edwards, M., Clark, C. W., Deng, L., Hagley, E. W., Helmerson, K., Rolston, S. L. and Phillips, W. D. "Imaging the Phase of an Evolving Bose-Einstein Condensate Wave Function." *Phys. Rev. Lett.*, 85, 2040 (2000).

[34] Jackson, J. D. Classical Electrodynamics. New York: Wiley (1999).

[35] Torii, Y., Suzuki, Y., Kozuma, M., Sugiura, T., Kuga, T., Deng, L. and Hagley, E. W. "Mach-Zehnder Bragg interferometer for a Bose-Einstein condensate." *Phys. Rev. A*, 61, 041602 (2000).

[36] Senaratne, R., Rajagopal, S., Geiger, Z., Fujiwara, K., Lebedev, V. and Weld, D. "Effusive Atomic Oven Nozzle Design Using an Aligned Microcapillary Array." *Rev. Sci. Instr.*, 86, 023105 (2015).

[37] Zwierlein, M. "Cooling and Trapping a Bose-Fermi Mixture of Dilute Atomic Gases." Diploma thesis, Massachusetts Institute of Technology.

[38] Guttridge, A., Hopkins, S., Kemp, S., Boddy, D., Freytag, R., Jones, M., Tarbutt, M., Hinds, E. and Cornish, S. "Direct loading of a large Yb MOT on the ${}^1S_0 \rightarrow {}^3P_1$ transition." *J. Phys. B.*, 49, 145006 (2016).

[39] Morice, O., Castin, Y. and Dalibard, J. "Refractive index of a dilute Bose gas." *Phys. Rev. A*, 51, 3896 (1995).